Variations in Subsidence along the Gulf of Mexico passive margin from Airborne-LiDAR data and Time Series InSAR in Louisiana

Carolina Hurtado-Pulido[1], Reda Amer[2], Cynthia Ebinger[1], and Hayden Holcomb[1]

[1]Tulane University
[2]Lamar University

November 24, 2022

Abstract

Coastal Louisiana is affected by sea level rates compounded by subsidence rates, leading to flooding and land loss. Subsidence in the region is caused by natural and anthropogenic processes that vary spatially and temporally across the Gulf of Mexico. Here, we quantify modern vertical and horizontal displacement using InSAR time-series and LiDAR differencing with data spanning between 1999-2020. Our study area is in Baton Rouge (BR), LA. It encompasses two Quaternary faults that cut cemented Pleistocene sediments. We test the ability of these methods to detect millimetric changes in an urban area with extraction and injection wells. Both methods indicate that the footwall of the BR fault has larger subsidence values (InSAR time series x=-0.552 to -0.732 mm/y) than the hanging wall of the fault (x=1.94 mm/y). LiDAR differencing accurately detects displacement trends, although it can overestimate the displacements. There are areas of uplift that spatially correlate to the locations of injection wells. Our results indicate that subsidence follows the spatial pattern of groundwater level changes proposed by previous studies, suggesting volumetric changes caused by fluid extraction and injection. The correlation of the BR fault zone with the boundary between blocks subsiding at different rates indicates that creep occurs along some sectors of the fault zone at rates of ~3 mm/y, similar to estimates from displaced structures. The creep may be accommodating changes in groundwater level rather than gravity and salt dynamics. The fault zones may be more permeable than surrounding areas, and more susceptible to hydrological and anthropogenic processes.

Hosted file

essoar.10512240.1.docx available at https://authorea.com/users/549761/articles/603717-variations-in-subsidence-along-the-gulf-of-mexico-passive-margin-from-airborne-lidar-data-and-time-series-insar-in-louisiana

Posted on 24 Nov 2022 — CC-BY-NC 4 — https://doi.org/10.1002/essoar.10512240.1 — This a preprint and has not been peer reviewed. Data may be preliminary.

Variations in Subsidence along the Gulf of Mexico passive margin from Airborne-LiDAR data and Time Series InSAR in Louisiana

Carolina Hurtado-Pulido[1], Reda Amer[2], Cynthia Ebinger[1], Hayden Holcomb[1]

[1]Department of Earth and Environmental Sciences, Tulane University.

[2]Lamar University, Beaumont, TX

Corresponding author: Carolina Hurtado-Pulido (dhurtadopulido@tulane.edu)

Key Points:

- Subsidence follows the spatial pattern of groundwater level changes from earlier studies, uplift areas spatially relate to injection areas
- The Baton Rouge fault shows creep that likely accommodates changes in groundwater level
- LiDAR differencing and SAR time series show similar vertical displacement trends. The former is less precise but finds horizontal changes

Abstract

Coastal Louisiana is affected by sea level rates compounded by subsidence rates, leading to flooding and land loss. Subsidence in the region is caused by natural and anthropogenic processes that vary spatially and temporally across the Gulf of Mexico. Here, we quantify modern vertical and horizontal displacement using InSAR time-series and LiDAR differencing with data spanning between 1999-2020. Our study area is in Baton Rouge (BR), LA. It encompasses two Quaternary faults that cut cemented Pleistocene sediments. We test the ability of these methods to detect millimetric changes in an urban area with extraction and injection wells. Both methods indicate that the footwall of the BR fault has larger subsidence values (InSAR time series $\bar{x}$=-0.552 to -0.732 mm/y) than the hanging wall of the fault ($\bar{x}$=1.94 mm/y). LiDAR differencing accurately detects displacement trends, although it can overestimate the displacements. There are areas of uplift that spatially correlate to the locations of injection wells. Our results indicate that subsidence follows the spatial pattern of groundwater level changes proposed by previous studies, suggesting volumetric changes caused by fluid extraction and injection. The correlation of the BR fault zone with the boundary between blocks subsiding at different rates indicates that creep occurs along some sectors of the fault zone at rates of ~3 mm/y, similar to estimates from displaced structures. The creep may be accommodating changes in groundwater level rather than gravity and salt dynamics. The fault zones may be more permeable than surrounding areas, and more susceptible to hydrological and anthropogenic processes.

Plain Language Summary

Coastal Louisiana is affected by sea level rise and surface sinking due to natural and human activities. We used aerial and satellite data to measure the amount of ground sinking and uplift between 1999 and 2020 in the metropolitan area of East Baton Rouge where sediments are stable and two geological faults are crossing the region. We found that the whole area is experiencing sinking, but the phenomenon is faster in the northern part than in the south of the study area contracting expecting natural behavior. Our results relate uplift to the location and distribution of wells injecting saline water and sinking relates to previous estimations of groundwater levels. Our results should be considered for future urban planning and water management.

1 Introduction

Climate change is modifying the natural systems of Earth. On a global scale, precipitation patterns have changed, increasing evapotranspiration, as sea level rises mainly by thermal and barystatic variations (Milliman and Haq, 1996; Frederikse et al., 2020). At local scales and particularly in coastal areas, steric variations contribute greatly to sea-level changes (Frederikse et al., 2020). At this scale, storm intensity and flooding increase as temperature rises (Milliman and Haq, 1996; Church et al., 2013). During the 20th century, the global sea level increased between 12-15 cm (Milliman and Haq, 1996), and it is expected to rise 65 ±12 cm by 2100 (Hoffman et al., 1983; Church et al., 2013; Nerem et. al., 2018). It will affect at least 190 million people living mainly in coastal areas (Kulp and Strauss, 2019).

Relative sea-level (RSL), which includes sea-level rise and subsidence effects, has increased along the Gulf of Mexico (GOM) coastline, causing great land loss. The mean RSL rate along the coast of Louisiana is 10 - 12 mm/y, which is higher than global average estimates of 1.2-3.3 mm/y (Penland and Ramsey, 1990; NASEM 2018a). Furthermore, the coast of Louisiana is predicted to suffer more adverse consequences than other areas along the GOM due to high rates of subsidence associated with the flood-controlled Mississippi delta (Pendleton et al., 2010). Subsidence rates may surpass sea level rise rates in some regions (Nienhuis et al, 2017; Karegar et al, 2020).

Subsidence in southern Louisiana is caused by anthropogenic and natural processes such as fluid extraction, compaction of recent sediments, isostatic adjustments, salt movement, and faulting (NASEM, 2018b) (Fig. 1). The GOM is bordered by thick sedimentary basins containing evaporites that overlie continental lithosphere stretched during Mesozoic time to form the continental margin. Previous studies have quantified subsidence caused by compaction and consolidation of compressible Holocene sediments of the Mississippi delta (e.g., Keogh and Törnqvist, 2019; Karegar et. al., 2020). Fault slip and creep are difficult to quantify because they can be episodic and slow, and the signal can be masked by faster processes such as sedimentation (Gagliano et al., 2003b). Other researchers quantified local subsidence related to the presence of fault traces and fluid extraction sites (e.g., Kuecher et al, 2001; Morton et al, 2002; Dokka, 2011). Mesozoic growth faults that detach in thick evaporite and shale horizons are common in Louisiana, and several show evidence for Holocene slip. Yet, there are only three instrumentally recorded earthquakes of M2.4-3.8 along the coastal fault systems (Stevenson and Agnew, 1985; Walter et al., 2016), suggesting that slip occurs primarily by creep. Despite the importance to infrastructure, there are just a few studies that have quantified fault slip rates and their relationship with subsidence at different time scales in the area, with rates ranging between 0.03 – 16.9 mm/y (Gagliano et al., 2003a, 2003b; Dokka et al., 2006; Shen et al., 2016; Culpepper et al., 2019a; Hopkins et al., 2021).

Differential movement along faults can be triggered in some areas by drivers such as extraction or injection of fluids. Wells in Louisiana have multiple purposes like water, gas and oil withdrawal, water injection and monitoring, with depths ranging between 4-6000 meters. There are a large number of wells that may induce fault movement (Morton et al. 2002; Chan and Zoback, 2007; Dokka, 2011; Jones et al., 2016). The change of pressure underground caused by fluid extraction or injection changes the volume at depth, which could influence fault activation (Kuecher et al., 2001). Multiple studies have related extraction of fluids with subsidence at different locations (e.g., Jones et al., 2016, Puskas et al., 2017; Li et al., 2020; Guzy and Malinowska, 2020), and uplifting with injection of fluids (Shirzaei et al., 2016; Teatini et al., 2011). Interferometric Synthetic Aperture Radar (InSAR) technology has been used previously to detect local and regional variations in ground elevation in areas across the GOM (Jones et al., 2016; Fiaschi and Wdowinski, 2020) and has been recommended by the NASEM (2018a). Other studies have used Light Detection and Ranging (LiDAR) data of two different surveys to perform differential LiDAR to find ground changes using different techniques such as Iterative Closest Point (ICP) and DEM differences (Nissen et al., 2012; Scott et al., 2018; Wheaton et al., 2010; Neverman and Fuller, 2016).

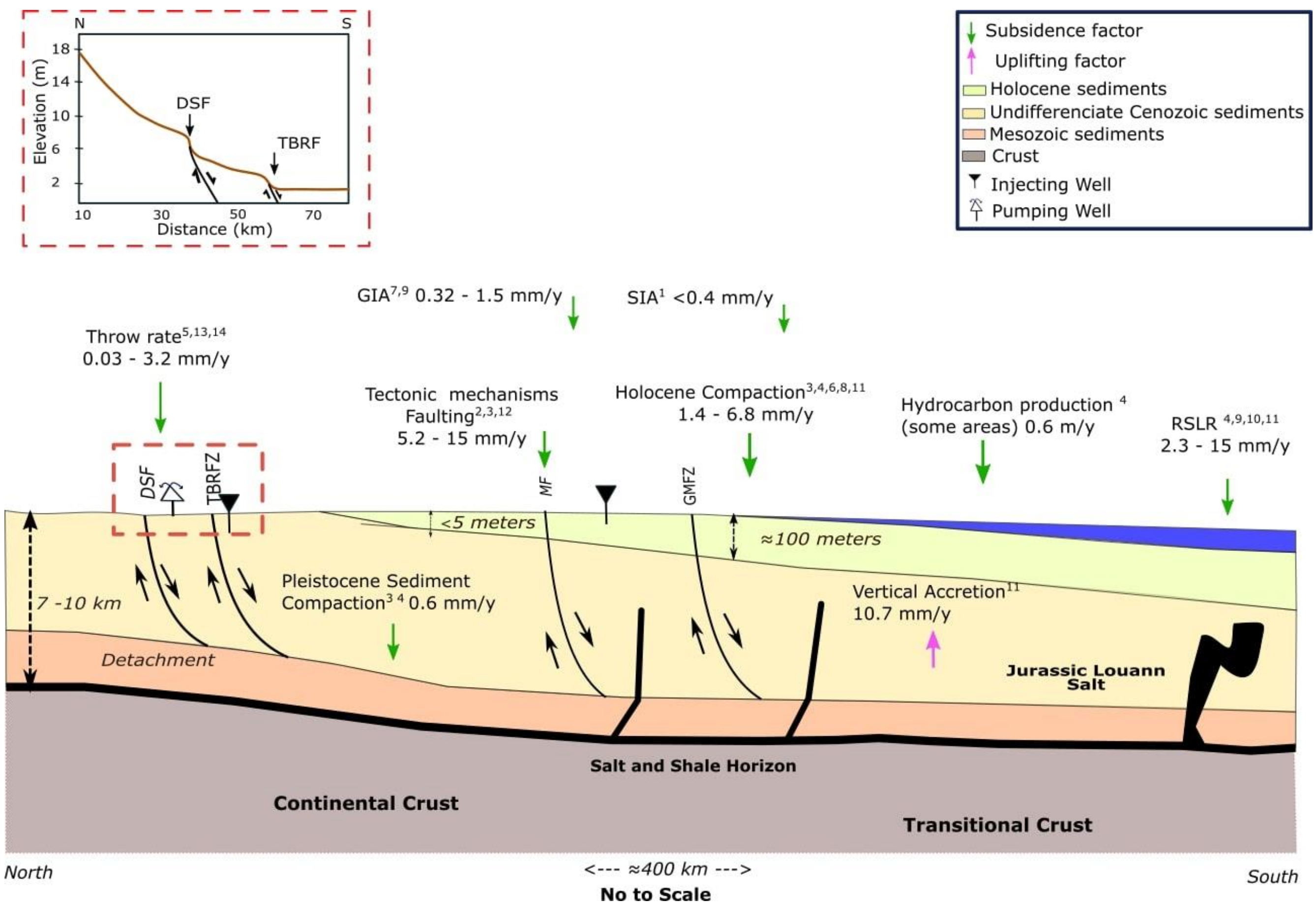

Figure 1: Schematic model of the extensional-contractional complex in southern Louisiana. After Shen et al. (2016) and Gasparini et al. (2015). Subsidence and uplifting references from: Kuchar et al. (2018)[1], Dokka et al. (2006)[2], Dokka, (2006)3, Chan et al. (2007)[4], Shen et al. (2016)[5], Keogh and Törnqvist (2019)[6], Love et al. (2016)[7], Karegar et al. (2020)[8], Karegar et al. (2017)[9], Penland and Ramsey (1990)[10], Jankowski et al. (2017)[11], Jones et al. (2016)[12], Penland et al. (2001)[13], Hopkins et al. (2021)[14].

In this research we use LiDAR and SAR data spanning 1999-2020 to answer the following questions: Assuming the 3 mm/y modern fault creep rate estimate by Hopkins et al. (2020) for the faults across Lake Pontchartrain at ~50 km of the study area (Fig. 2), is it possible to detect subsidence caused by fault slip with LiDAR and SAR? Are coastal growth faults slipping and causing subsidence? Are areas of slip near fluid extraction and/or urban development? We chose a test study area where two growth faults displace Pleistocene sediments and the influence of Holocene sediment compaction and cementation is small to isolate the signals of fault creep and anthropogenic change (e.g., Keogh and Törnqvist, 2019) (Figs. 1, 2). Considering that LiDAR and InSAR time series have been successful in other studies we decided to test LiDAR differencing in two faults in the Tepetate Baton Rouge fault system, the Denham Springs and the Baton Rouge faults using airborne LiDAR data that spans 1999 to 2018 (Figs. 1, 2). We use two LiDAR surveys to apply differencing and SAR data from Envisat and Sentinel-1 to apply Persistent Scatterer Interferometry (PSI). These techniques allow one to determine continuous surfaces of elevation change, which enable us to detect subsidence patterns in the study area. Comparing the results with well data, we can investigate where there is fault slip, and whether there is a spatial correlation between fault slip and injection and extraction wells over the last two decades. Answering these questions will let us verify or refute the following hypotheses: 1) Differencing LiDAR surveys of different time periods can detect small vertical motion signal with enough resolution of the two surveys, producing similar results to InSAR, assuming there is vertical displacement close to 3 mm/y as suggested by Hopkins et al. (2020) and 2) Tepetate Baton Rouge faults are slipping locally due to anthropogenic activities or by natural causes, or a mix of both.

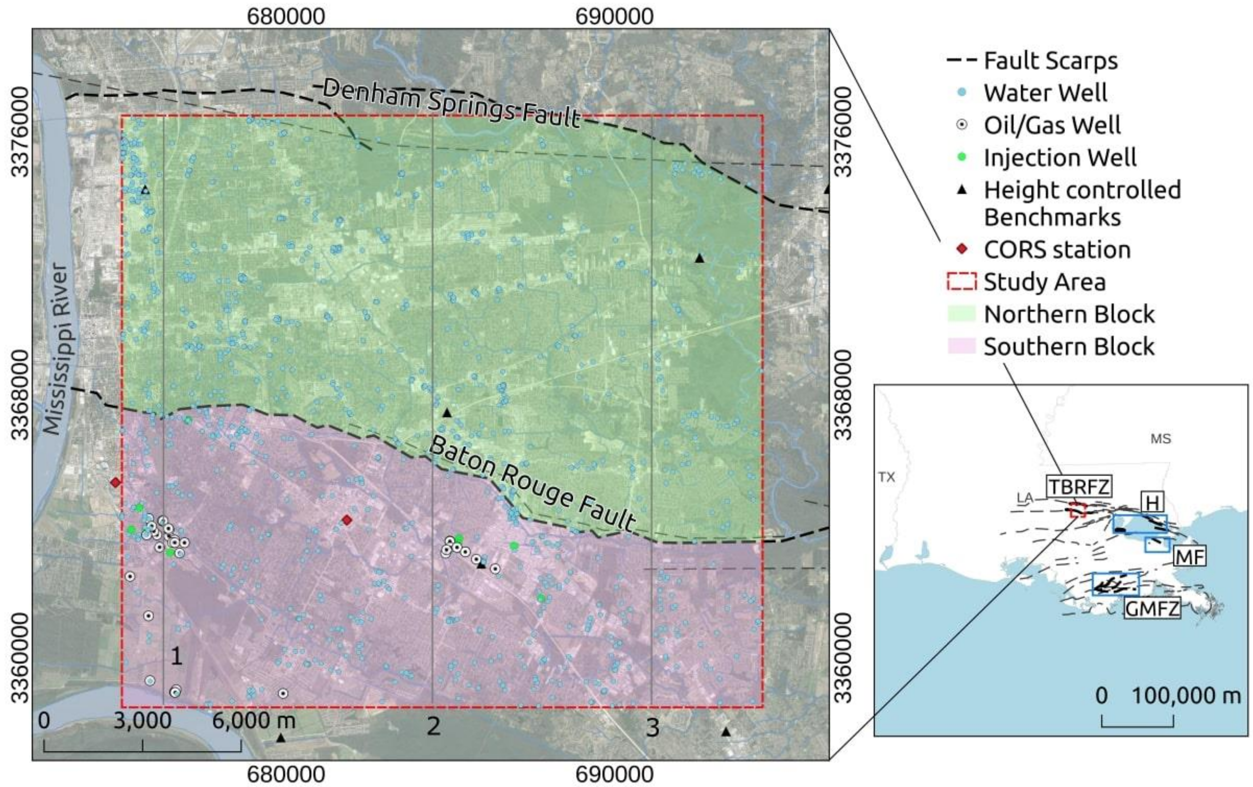

Figure 2: Study area. Inset shows the location of the study area with respect to the Mississippi delta, surrounding states, and main fault systems in Louisiana. Michoud fault (MF), Golden Meadow fault zone (GMFZ) and the faults used by Hopkins et al. (2021) (H) are shown. Fault scarps from Culpepper et al. (2019b). Well data from the Louisiana Department of Natural Resources (SONRIS), (n.d.). Heigh controlled benchmarks and CORS stations from the National Geodetic Survey (n.d.). Gray lines and numbers are profiles for figure S3. Base map imagery from QuickMapServices - QGIS (Map data ©2015 Google).

1.1 Background

The GOM is a passive margin that formed between 200-158 Ma when the Pangea supercontinent tore apart due to extensional forces that created multiple normal faults (e.g., Sawyer et al., 1991; Pindell and Kennan, 2009; Eddy et al., 2014). It is characterized by its bowl shape, low elevation coasts, broad continental shelf, followed by a steep continental slope, and a basin as deep as 4400 meters (e.g., Turner and Rabalais, 2019). The Mississippi River flows into the GOM, through the Mississippi delta (Figs. 1, 2). The delta began to develop at ~100 Ma with the formation of the Mississippi embayment, which concentrated sediment input to the gulf. During the last 7000 years, the delta depocenter relocated at least six times in response to climate and sea-level changes that occurred in the Holocene (Blum and Roberts, 2012). In the last 500 years, the Mississippi delta has suffered drastic land loss. This could lead to a shift of the depocenter of the Mississippi delta caused by sea-level rise, climate change, anthropogenic activities, and the lack of sediment delivery caused by artificial dams (e.g., Blum and Roberts, 2021).

Holocene sediment thickness increases from north to south and from west to east across the coast of Louisiana and it reaches a thickness of 100 meters at the shoreline (Penland and Ramsey, 1990). Processes such as compaction and compression of Holocene sediments are the primary factors causing subsidence on the Mississippi delta, and in areas close to the shoreline (Penland and Ramsey, 1990; Keogh and Törnqvist, 2019; Karegar et al., 2020). Keogh and Törnqvist (2019) and Jankowski et al. (2017) found that shallow subsidence occurring in the uppermost 5 meters in the Mississippi delta accounts for more than 60% of the total subsidence in the coastal area with rates varying between 6.4±5.4 and 6.8±7.9 mm/y. Hence, we focus on vertical crustal motions in areas north of the Holocene-Recent depocenter where compaction is minor and where fault slip can be isolated. Faults in the Mississippi delta are listric faults that commonly strike east-west (Dokka, 2011; Durham and Peeples, 1956; Culpepper et al., 2019). Likely, these faults were active until 40 Ma, but their rate of slip decreased between 25 Ma until the late Pleistocene (Shen et al., 2016). Our focus is the Tepetate-Baton Rouge fault system (TBRFS), which has three faults each of which have several meters of topographic relief (Fig. 3) (Denham Springs, Baton Rouge, and Scotlandville faults). These reactivated during the Pleistocene due to rapid sedimentation rates (Shen et al., 2016; Culpepper et al., 2019). The relief caused by Pleistocene-Recent slip along the TBRFS is clearly evident in DEMs produced from LiDAR data (Fig. 3). Faults in this system merge at a depth of 6 kilometers into a detachment that sits on an overpressured layer of salt and shale that dips with an angle between 45° to 65° (Gagliano, 2003a; Shen et al., 2016) (e.g., Fig. 2). Movement at depth of salt deposits and sediments can reactivate some fault segments (Gagliano et al., 2003a).

Studies differ in the importance of faulting as a factor causing subsidence in southern Louisiana. Shen et al. (2016) calculated mean fault throw rates in the eastern portion of the TBRFZ using optically stimulated luminescence dating to measure offset times and boundaries of offset of fluvial/deltaic sediment facies. Their results indicate that faulting in the TBRFZ is not a dominant process contributing to subsidence, given that the faults have an average slip ranging between 0.02 -0.07 mm/y for areas lying on Pleistocene sites during the last 103 to 105 years. However, there is visual evidence of building and road displacements along the TBRFZ and other coastal faults with measured rate estimates of ~3 mm/y (McCulloh, 2001; Hopkins et al., 2021). Dokka et al. (2006a, 2006b) interpreted episodes of subsidence along the Michoud fault (MF) between 1955 to 2005 as evidence of episodic fault slip, although it could also be caused by groundwater extraction (Jones et al., 2016). Fault motion and subsidence near the Golden Meadow fault zone (GMFZ) have been related to hydrocarbon extraction in some studies (Morton et al., 2002; Chan and Zoback, 2007).

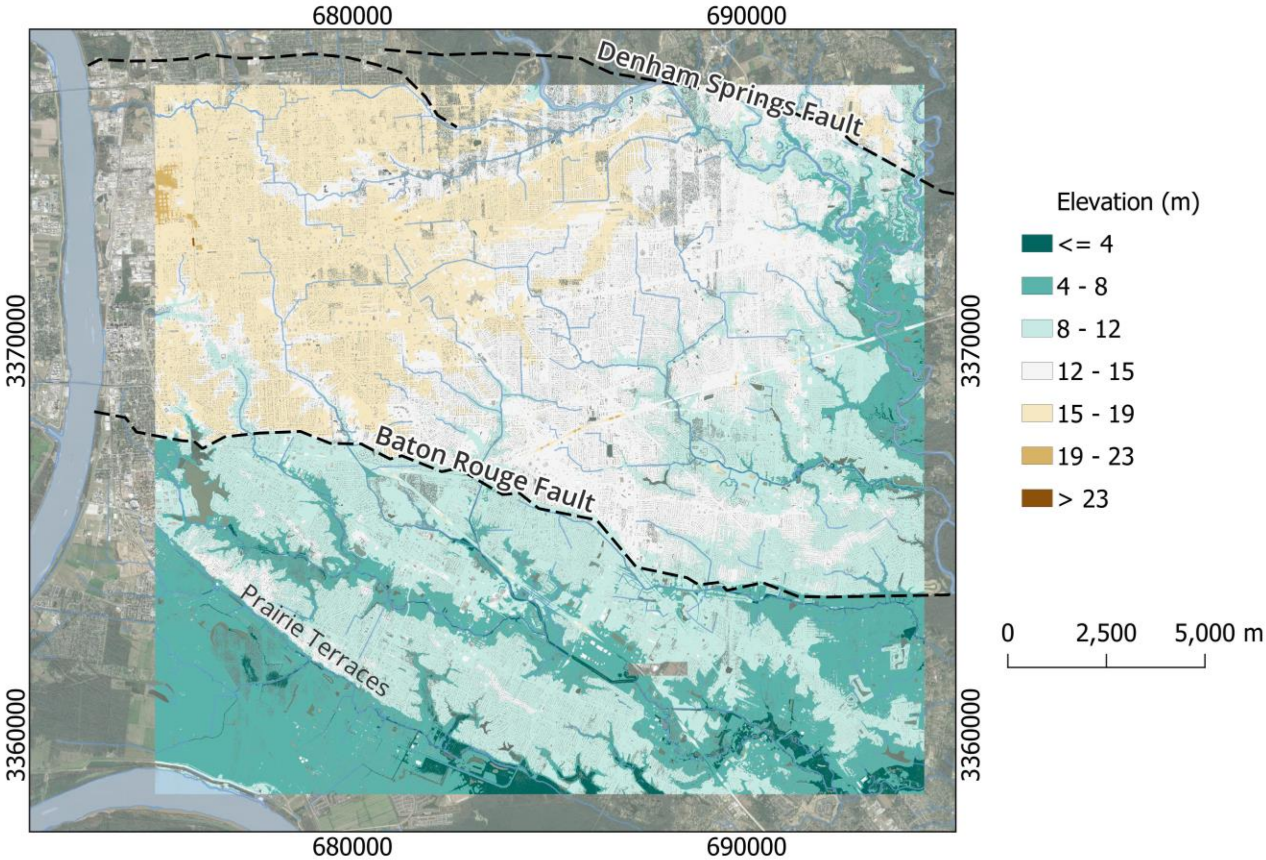

Figure 3: Digital Elevation Model from the study area showing the topographic relief across the Denham Springs and East Baton Rouge faults (dashed lines). The geological contact labeled as the Prairie Terraces marks the edge of the natural levee in the area. Created using LiDAR point cloud from 2018. Base map imagery from QuickMapServices - QGIS (Map data ©2015 Google)

Glacial Isostatic Adjustment (GIA) and Sediment Isostatic Adjustment (SIA) may lead to long-term subsidence along the east coast of North America (Karegar et al., 2017). GIA was modeled using RSL data from tide gauges and vertical and horizontal velocities from GNSS from 2006-2015 along the East and Southeast coast of the United States by Love et al. (2016). During this century GIA in south-east Louisiana will contribute approximately 30 mm to RSL rise with a rate of 0.32 mm/y (Love et al., 2016). On the other hand, SIA registers a rate of less than 0.5 mm/y on areas with thicker Holocene sediments (Wolstencroft et al., 2014).

The aquifer system in Baton Rouge is part of the Southern Hills aquifer and the Mississippi River Alluvial aquifer (Tomaszewski et al., 2002). The former is composed of interbedded layers of compressed clay/silt and layers of porous sands. The sands south of the Baton Rouge fault are more continuous than in the north area of the fault (Vahdat-Aboueshagh and Tsai, 2021). These sands form ten independent aquifers named after their depth under the Baton Rouge industrial district, with depths between 400-foot to 2700-foot (Tomaszewski et al., 2002). Large volumes of groundwater removal have affected reservoirs in the Baton Rouge area (White, 2017). Groundwater level has decreased forming cones of depression at local and regional scales (White, 2017), and saline water from southern areas has intruded into some of these sands (Nasreen, 2003; Elshall et al., 2013). Deep aquifers have larger withdrawal volumes, and, therefore, have been more affected during the last decades (Tomaszewski et al., 2002; Nasreen, 2003). The Mississippi River Alluvial aquifer has not had a significant groundwater level decrease, and saline water has not infiltrated the eastern portion of the aquifer where the study area is located (Tomaszewski et al., 2002; Nasreen, 2003). The Baton Rouge fault plays an important role in the dynamics of the aquifers in Baton Rouge; it is a barrier for saline water coming from the southern area, but it may serve as a conduit and can allow lateral intrusions due to pumping of groundwater at the north of the fault (Nasreen, 2003; Elshall et al., 2013; Anderson et al., 2013). The Denham Springs fault is permeable and allows freshwater to flow down it to the south, where pressure gradients cause southward flow and aquifers in the area between the two faults recharge (Elshall et al., 2013).

2 Data

Airborne LiDAR is a technique that uses laser light pulses directed towards Earth’s surface to measure the time of pulse return. This time is used to calculate the distance between the sensor and the surface. Airborne LiDAR is used along with an airborne Global Navigation Satellite System (GNSS) to know the location of the sensor while surveying and an Inertial Measuring Unit (IMU) to know the angular orientation of the sensor relative to the ground (Lillesand and Kiefer, 2000). SAR is a technique to capture data using microwave wavelengths. The sensor on board the satellite or aircraft sends and receives signals that can penetrate haze, clouds, snow, and smoke depending on the wavelength. SAR is particularly useful because it simulates a longer antenna enabling the possibility of using long wavelengths and improving spatial resolution (Lillesand and Kiefer, 2000; Chan and Koo, 2008). We utilize two data sets spanning the longest time periods possible to detect vertical and horizontal land motion associated with natural and anthropogenic processes in southern Louisiana.

2.1 SAR data

SAR datasets were captured by the EnviSAT and Sentinel-1 satellites. Both capture data on the C-band (5.405 cm), produce Single-Look Complex images, we used vertical transmit and receive polarization (VV). The EnviSAT dataset was collected between 2004 and 2010 and it is composed of 23 scenes, this satellite has a mean incidence angle of 18, pixel dimensions of 5x25 m and has an altitude of 800 km (ESA, 2021a). The Sentinel-1 dataset was collected in Interferometric Wide mode between 2017 and 2020 and consists of 33 scenes, Sentinel-1 has an incidence angle between 37-39° and pixel dimensions of 14.1x2.3 m, and orbits at an altitude of 693 km (ESA, 2021b). Each of these datasets created a different time series that was analyzed separately. For images list is on Table S1.

2.2 LiDAR data

LiDAR point clouds come from two surveys that cover the portion of the TBRZ fault located in the East Baton Rouge parish in southern Louisiana. The first dataset was collected in March of 1999, has a point space of 4 m, a pulse rate of 15 kHz and a vertical accuracy measured as the Root Mean Square Error (RMSE) of 15 cm (USACE, 2001). The newest was collected between March and April of 2018, has a point space of 0.33 m, a pulse rate of 450 kHz and a vertical accuracy of RMSE=3.6 cm (USGS, 2019). For more details see Table S2.

3 Methods

3.1 Persistent Scatter Interferometry - PSI (time series InSAR)

PSI is a differential InSAR technique that allows one to use the phase information from multiple SAR images captured at different times to estimate phase changes between several interferograms. Phase change information is used to calculate the velocity of displacement and the displacement time-series during the study period (Hooper et al., 2004; Crosetto et al., 2016). PSI uses pixels with low phase noise, called Persistent Scatterers, across lengthy time intervals in multi-temporal data (Ferretti et al. 2001; Crosetto et al., 2016). This technique is particularly useful in urban areas that have a high density of persistent scatterers (e.g., Jones et al., 2016; Fiaschi and Wdowinski, 2020). Displacement is calculated on the Line of Sight (LOS), projecting 3D displacements into 1D displacements in the LOS direction (Crosetto et al., 2016). One of the advantages of this technique is its ability to detect signals of ground displacements of <10 mm/y (Lyons and Sandwell, 2003).

A brief description of this technique follows (L3Harris, 2014; 2021). One of the SAR images from the stack is selected as a reference to co-register the other images and to create the time series. Then, the interferometric process is implemented. This step includes co-registration and interferogram generation between the reference image and the other images in the stack, as well as interferometric flattening, where each interferogram is flattened. The topographic phase component is prepared using a DEM to be subtracted from the total interferometric phase. Then, reference points, which are persistent scatterers, are chosen using the Amplitude Dispersion Index, defined as the temporal average amplitude of a pixel over temporal standard deviation of the amplitude of a pixel.

After these preparation steps, the first inversion step is executed. This step calculates displacement velocity and residual height using a linear model for each pixel in the area with respect to the reference points selected above. The model estimates are removed from all the interferograms to recalculate velocity and residual height. Next, the second inversion is applied. At this step the atmospheric phase is estimated using a low and a high filter to remove spatial and temporal variations caused by the troposphere from the interferometric phase. Next, displacements are calculated from the clean interferometric phase for each interferogram. The estimates for displacement and residual heights are recalculated and just pixels with coherence larger than 0.66 (low phase noise) remain. The results are geocoded and exported to raster and vector files.

We used SARscape software (version 5.6; 2021) to calculate vertical displacement velocity for both datasets. The topographic phase was removed using the Shuttle Radar Topography Mission (SRTM) DEM, which has a spatial resolution of 30 m. To reduce decorrelation noise and build the spatial coherence map we ‘multilooked’, the data in azimuth and range directions as follows. For the EnviSAT dataset we used four azimuth-looks and one range-look; for the Sentinel-1 dataset we used five azimuth-looks and one range-look. This recombination reduces the quantity of data to be processed but also decreases the spatial resolution (Goldstein et al., 1988). Only pixels that fulfilled these threshold parameters were selected: 30% overlap for sub-areas, a single reference point per 5 km2, and coherence larger than 0.66. The PSI displacements are calculated in the LOS direction. Then, we converted these to vertical displacements using the incidence angle given as one of the results during the PSI process for each point. We assume that the Earth's curvature does not affect the measurements.

3.2 LiDAR co-registration

Co-registration of the LiDAR point clouds is the process of aligning datasets acquired at different times over the same area. Knowledge of the magnitude and the direction of the misalignment enables us to detect horizontal displacements and correct the geographical location of the point clouds to do vertical differencing between corresponding points. Misalignments between the point clouds are caused by: 1) distortion of the point clouds from measurement error related to flight discrepancies; 2) real changes in the landscape (subsidence, uplift, translation, vegetation growth, mass movement); and 3) local topographic relief on flat surfaces where there is less random LiDAR scattering (Scott et al., 2018).

Point cloud co-registration is done in two ways: using only LiDAR ground points and using LiDAR points from structures that should be stable over time (e.g., flat roofs, parking lots, and highways - Fig. 4). Ground points were taken using the original classification of both point clouds done by the distributors. A feature-based technique allows us to take information from structures that are expected to be stable and use them as control points (Brook and Ben-Dor, 2011). Using PDAL filters (Point Data Abstraction Library, 2018) we created a new point cloud for each dataset whose points only belong to structures that satisfy specific criteria. First, the point must be in a plane. To evaluate this criterion, we used the filter "estimaterank", which categorizes each LiDAR point in a line, plane, or a 3D structure. The threshold value defines whether a point is linearly independent or not. We used "estimaterank" with 14 neighbors and a threshold value of 5 for the 1999 dataset and 1 for the 2018 dataset. Secondly, the points must be in an elevation range assigned depending on if they are in the hanging wall or footwall of the Baton Rouge Fault. The range for the hanging wall is 7 to 35 m and for the footwall is 12 to 35 m. These values were chosen from observation of the LiDAR data, using the maximum value from tall buildings and the lowest from roads and parking lots. DEMs show that there are at least ~5 m of relief along the Baton Rouge fault (Fig. 3), therefore, features on the hanging wall are expected to be at a lower elevation.

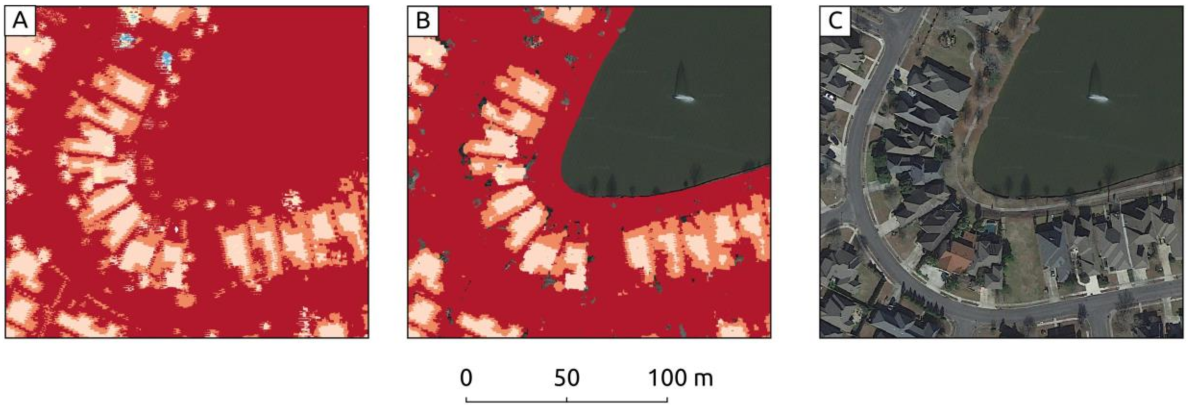

Figure 4: Example of stable surfaces from 2018 LiDAR point cloud. **(a)** Original point cloud, **(b)** Chosen stable surfaces, **(c)** Reference image of the area. Base map imagery from QuickMapServices - QGIS (Map data ©2015 Google)

3.3 Iterative Closest point – ICP

This algorithm allows one to perform 3D LiDAR differencing by calculating rotations and translations of the surface (Scott et al., 2018; Nissen et. al., 2012). The ICP algorithm aligns user-defined core points in the point clouds of two datasets. Each core point is defined by a grid of 50 m and centered in a square or window of 50x50 m in the 1999-point cloud and 51x51 m in the 2018-point cloud. We chose these values for computational optimization. The horizontal coordinates of each core are the central point in each window, and the elevation value is the average of all the points in the window. ICP assumes that each window behaves as a rigid body (Nissen et. al., 2012).

This algorithm iterates as follows: 1) Finds the closest core point in the old point cloud for each core point in the new point cloud, 2) Calculates translation and rotation of each core point in the old point cloud, 3) Iterates until a minimum distance is reached or until a certain number of iterations are completed (Scott et al., 2018; Nissen et. al., 2012). We iterated until the translation was less than 10-4 meters or when 10 iterations were completed. ICP applies a linear transformation to the old data to have the best alignment possible. It finds the rigid body transformation matrix, with α,β and γ representing the rotations on the x, y, and z axes, and t_x,t_(y,) t_z representing the translations in the same three axes in equation 1 (Scott et al., 2018).

$$\boldsymbol{NewestPointCloud \approx TransformedOldpointcloud} = \begin{pmatrix} \mathbf{1} & -\boldsymbol{\gamma} & \boldsymbol{\beta} & \boldsymbol{t_x} \\ \boldsymbol{\gamma} & \mathbf{1} & -\boldsymbol{\alpha} & \boldsymbol{t_y} \\ -\boldsymbol{\beta} & \boldsymbol{\alpha} & \mathbf{1} & \boldsymbol{t_z} \\ \mathbf{0} & \mathbf{0} & \mathbf{0} & \mathbf{1} \end{pmatrix} \boldsymbol{Oldpointcloud} \qquad (\boldsymbol{Eq}.\mathbf{1})$$

We run the ICP algorithm with LiDAR ground points and with LiDAR points from stable surfaces chosen in the co-registration process. In both cases, approximately 122,400 core points were created. The results of each core represent the displacement of a window. These results were filtered to have only displacements between 0 to 1 m to eliminate outliers showing artifacts (e.g., new constructions), and not natural displacements. Then, results were averaged to have a representative point per 2.25 km2. The error for this process is given initially by the Point-to-Plane error metric (Scott et al., 2018; Nissen et. al., 2012), and the final averaged results were evaluated using a margin of error metric of 95%. To perform differencing, we use the 3D_Differencing MATLAB code created by Scott et al., (2020) to apply ICP to topographic data, and LIBICP (LIBrary for Iterative Closest Point fitting) software created by Geiger et al. (2011) to solve the rigid body transformation.

3.4 Vertical DEM differencing

To do vertical differencing we used Geomorphic Change Detection (GCD) software. It allows one to detect topographic and volumetric changes using digital elevation models (DEM) (Wheaton et al., 2010). With GCD we created a DEM of Differences (DoD) doing pixel by pixel differentiation. The vertical accuracy of these is given by standard error propagation and depends on the accuracy of the original point clouds (Wheaton, 2018). To implement GCD, the DEM derived from the LiDAR point clouds is created using the PDAL filter "filters.range", which separates LiDAR points classified as ground from other levels, and then rasterizes this subset of data using GDAL. We created the DEMs using the IDW (Inverse Distance Weighting) interpolation technique, which is a linear combination of the samples, which weights them by their distance to the point of interest. A radius can be used to choose only close points (Shepard, 1968; Polat et al., 2015). We used a pixel size of 5 m, and a radius of 5 m for the 1999-point cloud and 3 m for the 2018-point cloud. The radius is different to ensure that the DEMs from 1999 have enough points to interpolate. We used a power parameter equal to 2 because it has been shown to produce good empirical results and it is computationally efficient (Shepard, 1968). The error of each DEM with respect to the original LiDAR data was estimated using the root mean square error metric.

4 Results, or a descriptive heading about the results

4.1 Velocities from InSAR time series – Envisat and Sentinel-1

The footwall of the Denham Springs fault does not show any results in the InSAR-time series from Sentinel-1 (Fig. 5A), and the results from the EnviSAT are very noisy (Fig. 6). This area is noisy in InSAR time series because most of the terrain is covered by vegetation and there are not enough persistent scatterers (Fig. 5B).

For case of discussion, we will call the footwall block of the Baton Rouge fault northern block, and the hanging wall of the Baton Rouge fault the southern block as indicated in Figure 1. Results from InSAR time series using Sentinel-1 data captured between 2017 and 2020 indicate that the northern block is moving in opposite sense to the long-term fault displacement, in other words the subsidence rates in this block are larger than the ones found for the southern block (Fig. 5A). Areas labeled as Agricultural, or Park/Water in Figure 5B do not have enough persistent scatterers; therefore, we cannot produce results over these areas with this method. We calculated a mean velocity value of -0.732±0.004 mm/y for the northern block, which indicates that subsidence dominates the block. The southern block has a mean velocity value of

1.890±0.008 mm/y indicating that uplifting dominates the area. Errors in this section are presented as a margin of error within a confidence interval of 95%.

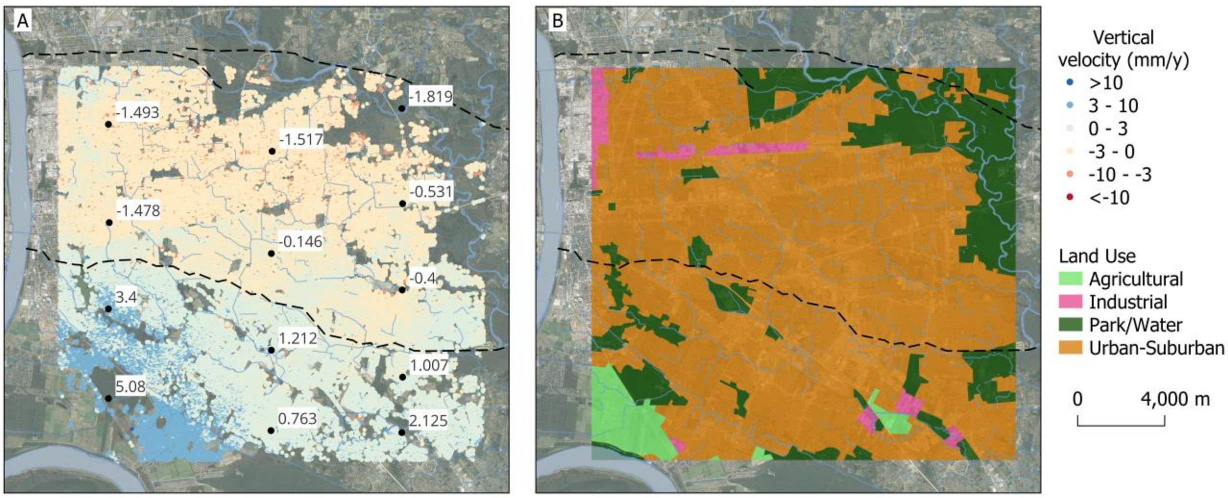

Figure 5: Results from Sentinel-1 compared to Land use. **(a)** Vertical displacement rates calculated with PSI method. Labels on the image indicate mean vertical rates for the black dots. Negative velocities indicate subsidence while positive rate indicate uplifting. **(b)** Land uses. We mapped land uses using the basemap imagery from QuickMapServices - QGIS (Map data ©2015 Google.) at a scale of 1:10.000.

Figure 6 shows the spatial patterns of vertical displacement between 2004 and 2010 calculated with EnviSAT data. The results are noisy in many parts of the area, although we can see some patterns. The northern block has mean velocities of -0.552 ±0.035 mm/y, indicating that most areas here are subsiding. On the other hand, the southern block has positive rates indicating uplift, with mean velocities of 2.007±0.055 mm/y. The noise on the EnviSAT results may be caused by the resolution of the data and the lack of persistent scatterers in during the study period. It also may be related to land-use changes during that period after Hurricane Katrina in 2005. This will be further explained in the discussion section.

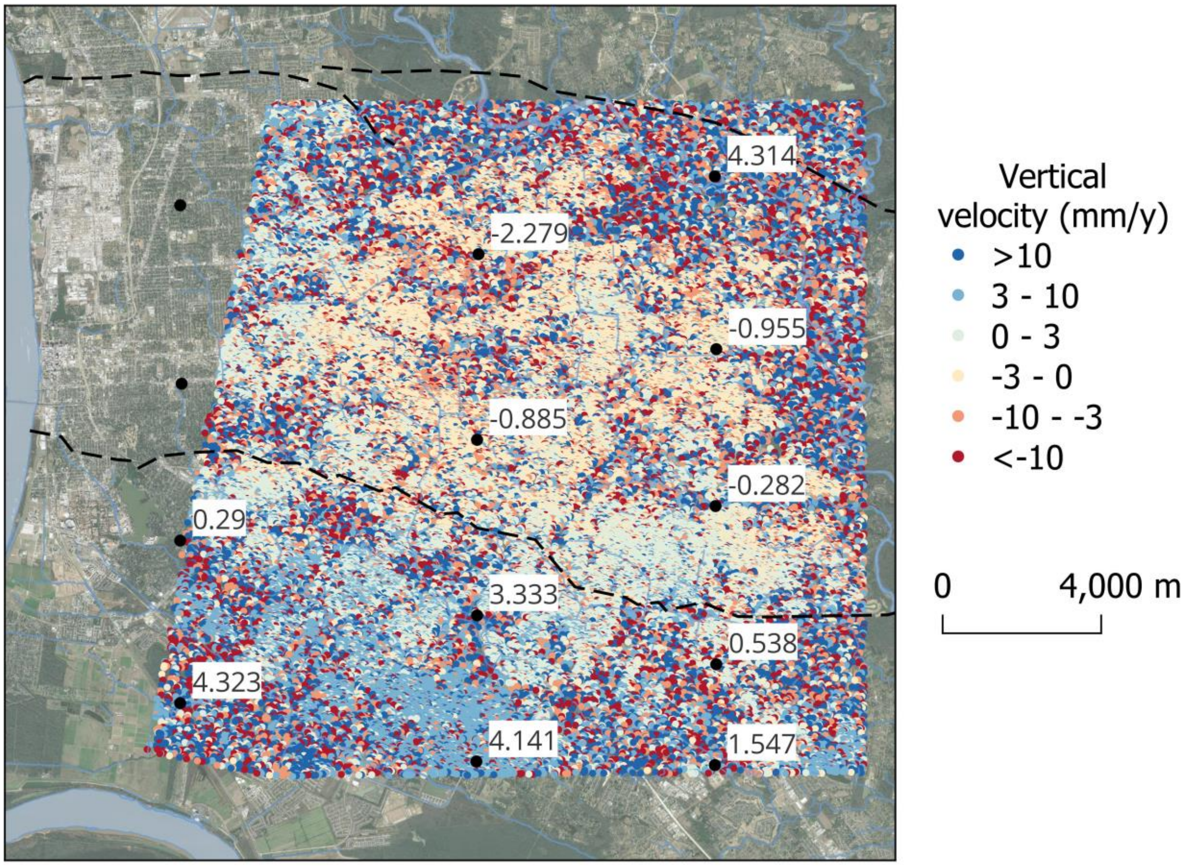

Figure 6: Vertical displacement rates calculated with PSI method using EnviSAT data. Labels on the image indicate mean rates for the black dots to indicate how subsidence change over the area

4.2 Horizontal displacement from ICP (Iterative Closest Point)

Overall, ICP indicates that between 1999-2018 the area is moved towards the southeast direction (Fig. 7). Results using the two different LiDAR classifications – ground and stable surface points – have different spatial behaviors. Horizontal displacement calculated with ground LiDAR points (Fig 7A) is spatially more homogenous in the whole area. Using ground points, we estimated that between 1999 and 2018, the mean displacement of the southern block was 148±11 mm towards the east and 85±8 mm towards the south. The northern block has a mean displacement of 145±10 mm to the east and 110±9 mm to the south.

The horizontal displacement calculated with stable LiDAR points shows different behaviors on each of the blocks (Fig. 7B); First, the southern block seems to be moving faster than the northern block with mean displacements of 178±21 mm to the east and 91±13 mm to the south, while the northern block had mean displacements of 121±14 mm to the east and 81±13 mm to the south. One particular feature of these results is that the areas closer to the eastern section of the Baton Rouge fault show large spatial variability and have larger errors. A caveat of using only stable surface points is that the number of these points is small, affecting mostly the oldest LiDAR survey.

Our results agree with the general estimated direction of displacement calculated with the two CORS stations in the study area (Fig. 7, Table 3). Between 1999 and 2018, the mean displacement with GNSS has a magnitude of approximately 239.21 mm to the east and 11.97 mm towards the south. Our results also indicate large displacement towards the east (148-178 mm), but displacements ~10 times larger towards the south (81-85 mm) for the study period.

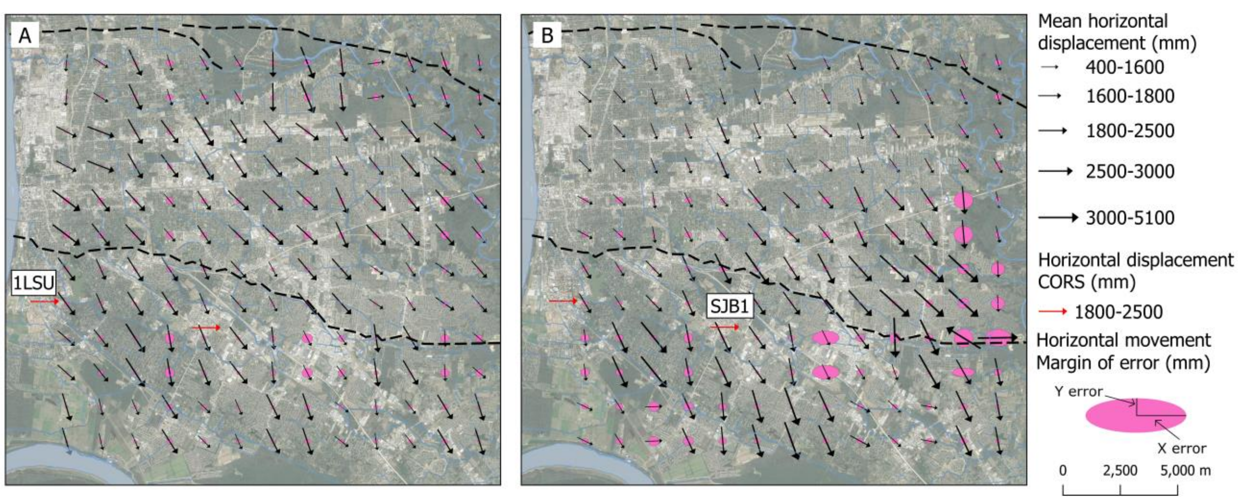

Figure 7: Horizontal displacements calculated from ICP algorithm. **(a)** Horizontal displacements using ground LiDAR points. **(b)** Horizontal displacements using stable surface LiDAR points. Each black arrow represents the average displacement of an area of 2.25 km^2. Arrow directions represent the mean displacement direction, and the length of the arrow represents the mean displacement magnitude. Ellipses show the error multiplied by 30 for visualization, where X-error represents the error to the east and Y-error represents the error to the south. Errors are calculated as the margin of error with respect to the mean with a 95% of confidence limit. Red arrows are the horizontal displacement using the rates from the GNSS CORS stations for 19 years (1LSU, Vx=-12.9±0.39 mm/y,

Vy=-0.54±0.3 mm/y; SJB1, Vx=-12.37±0.23 mm/y, Vy=-0.69±0.29 mm/y). GNSS information from Nevada Geodetic Laboratory GPS Network Map (Blewitt et al., 2018; UNAVCO, 2006), last access on December 6, 2021.

4.3 Vertical displacement from LiDAR

Both methodologies used to calculate vertical displacement with LiDAR data give us similar results: subsidence is occurring across the study region, with larger subsidence in the northern block. Uplifting regions are present in the southern block in the same areas that InSAR time series shows them (Figs. 5, 6, 9, 10). Results from the ICP algorithm, where each point in Figure 8 represents the estimated displacement for an area of 2.25 km2, shows that subsidence increases from southwest to northeast. Using LiDAR ground points (Fig. 8A) there is no uplifting in large regions as shown with PSI (Figs. 5, 6). The subsidence displacements in the southern block are smaller in comparison to the displacements in the northern block. The mean vertical displacement on the southern block is -131±8 mm, and on the northern block is -193±14 mm. Now, using stable LiDAR points, we see some areas of uplift mostly on the southern block, and again we estimate more subsidence in the northern block. The mean vertical displacement in the southern block, in this case, is -103±28 mm and on the northern block is-156±20 mm. These errors are margin of error within a confidence interval of 95%. ICP results are close to the estimate displacement calculated with GNSS using the two stations in the southern block (-44.365 mm using a vertical displacement mean rate of -2.355 mm/y, Fig. 8), assuming that the vertical rate has been constant over time.

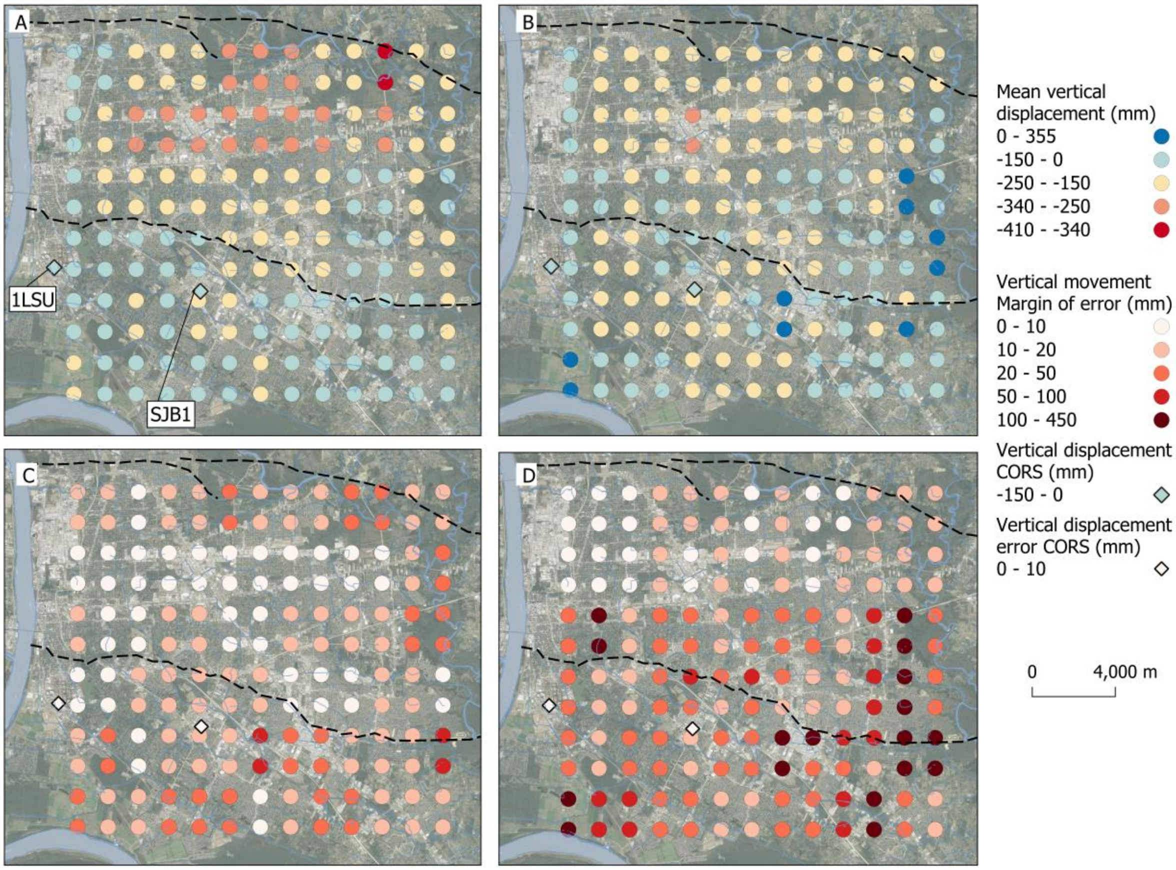

Figure 8: Vertical displacement calculated from ICP algorithm. **(a)** Vertical displacements using ground LiDAR points, **(b)** ICP displacements using stable surfaces LiDAR points, **(c)** Margin of error in the vertical direction for (a), **(d)** Margin of error in the vertical direction for (b). Each circle represents the average displacement of an area of 2.25 km^2. Errors are calculated as the margin of error with respect to the mean with a 95% of confidence. Rhombus are the vertical displacement calculated using rate from the GNSS CORS stations for 19 years (1LSU, Vz=-3.86±0.84 mm/y; SJB1, Vz=-0.85±0.79 mm/y). GNSS information from Nevada Geodetic Laboratory GPS Networks Map (Blewitt et al., 2018; UNAVCO, 2006), last access on December 6, 2021

We calculated LiDAR differencing with GCD without co-registration, with co-registration using ground points, and with co-registration using stable surface points. The mean estimates for vertical displacement without any co-registration for the 19 years were larger than 300 mm and we obtained more extreme values, which are not coherent with other estimates nor the features of the area. Therefore, we only keep the results from co-registered DEMs. We are presenting here just the results from LiDAR differencing co-registered with ground points (Fig. 9) because in these results are similar to the results from co-registration with stable points. In this case, we estimated a mean vertical displacement of -118±0.00025 mm on the southern block, and -196±0.00015 mm for the northern block. These errors are margin of error within a confidence interval of 95% and are small due to number of pixels in each block. Empty pixels on Figure 9 do not have results because there are water bodies, high vegetation density, or the values were below the propagated error calculated for each subarea of 2.25 km2. Insets show areas of interest that will be discussed in the next section.

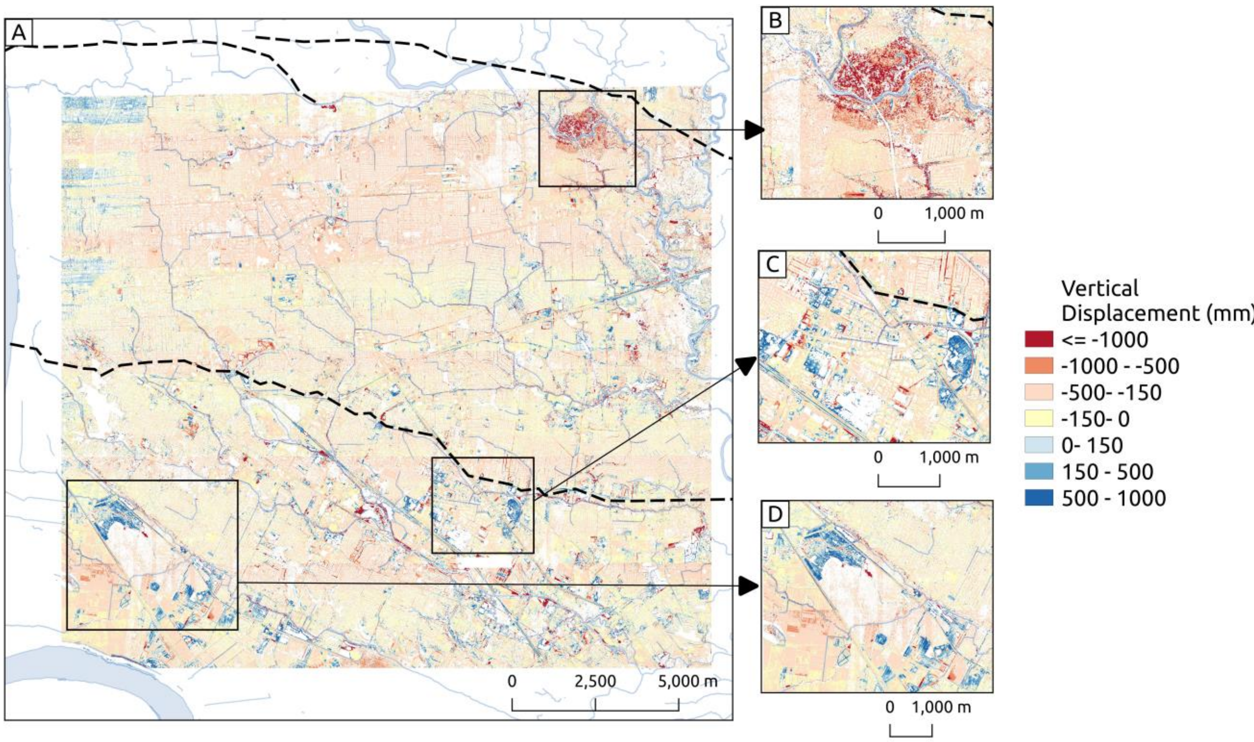

Figure 9: Vertical displacements from LiDAR differencing using GCD. **(a)** Vertical displacement calculated using the DEM co-registered using the results from ground points co-registration for the complete study area. **(b, c, d)** Some areas of interest discussed in text.

All our estimations and main statistics are summarized in Table 1 below.

Table 1: Main statistics for PSI rates, LiDAR differencing from ICP and GCD and GNSS. MOE stands for Margin of Error.

PSI – Estimate vertical displacement rates						
Dataset	**Time span**	**Block**	**Mean (mm/y)**	**Median (mm/y)**	**MOE (mm/y)**	**Mean displacement (mm)**
EnviSAT	2004-2010	Northern	-0.552	-0.872	0.035	-3.864
		Southern	2.007	2.179	0.055	14.049
Sentinel-1	2017-2020	Northern	-0.732	-0.726	0.004	-2.928
		Southern	1.890	1.667	0.008	7.56

ICP – Estimate displacement (1999 -2018)						
Point cloud	**Variable**	**Block**	**Mean (mm)**	**Median (mm)**	**MOE (mm)**	**Mean rate (mm/y)**
Ground	Vertical	Northern	-193	-175	14	-10.178
	X (east)		145	141	10	7.642
	Y (south)		-110	-112	9	-5.782
	Vertical	Southern	-131	-138	8	-6.879
	East		148	151	11	7.789
	South		-85	-90	8	-4.471
Stable	Vertical	Northern	-156	-177	20	-8.213
	X (east)		121	102	14	6.389
	Y (south)		-81	-59	13	-4.252
	Vertical	Southern	-103	-143	28	-5.429
	X (east)		178	177	21	9.366
	Y (south)		-91	-95	13	-4.770

GCD – Estimated vertical displacement (1999 -2018)				
Block	**Mean (mm)**	**Median (mm)**	**MOE (mm)**	**Mean rate (mm/y)**
Northern	-196	-192	0.00015	-10.339
Southern	-118	-153	0.00025	-6.194

GPS –Rates and displacements (1999-2018)			
Mean rate - vertical (mm/y)	-2.335	**Mean displacement vertical (mm)**	-44.365
Mean rate - X (mm/y)	12.59	**Mean displacement X (mm)**	239.21
Mean rate - Y (mm/y)	-0.63	**Mean displacement Y (mm)**	-11.97

5 Discussion

5.1 InSAR time series and LiDAR differencing measurements

InSAR time series created with the PSI method calculated rates of displacement in the LOS direction. We translated LOS displacement to vertical displacement using the incidence mean angle for each point in the results. This technique uses persistent scatterers on the surface, making this methodology appropriate for urban environments with a high density of scatterers, such as Baton Rouge. One must be cautious, however, with the interpretation of these results because they incorporate the signal of all processes affecting the persistent scatterers (Jones et al., 2016). Each time-series was calculated using images from different dates; therefore, vertical displacement rates may be affected by seasonal variations from the hydrological cycle (e.g., Li et al., 2020). Most of the images that we used from EnviSAT and Sentinel-1 were captured during dry periods in Baton Rouge (September to May) and some from wetter periods. If there is any elastic deformation caused by seasonal changes in water mass, it would be more positive than negative due to the time distribution of the images. Seasonal loading, therefore, may contribute to the observed uplift in the southern block for both time series (Fig. 5 and 6). If the observed uplift of our results is caused by seasonal rebound, then subsidence rates may be larger than the ones reported with InSAR time series, this based in comparison to hydrological models (e.g., Puskas et al., 2017).

We also used two LiDAR surveys captured over similar seasonal conditions to perform LiDAR differencing (Table 2). Therefore, this method probably measured net changes between both surveys, although uncertainties in each survey must be considered. In this case, the survey taken in 1999 affects the displacement estimates more than the survey from 2018 due to the sparsity of the point cloud. LiDAR allows one to use data from surfaces of interest such as ground and stable surfaces points separately. The advantage of using different LiDAR points is shown in Figures 7 and 8, where surfaces that are at different elevations or anchored in the subsurface report distinct behavior of displacement in some zones of the study area. The estimated horizontal displacement indicates that the study area moves towards the southeast in both blocks (Fig. 7) agreeing with the geological characteristics of listric faults across the gulf (Culpepper et al., 2019). Nevertheless, horizontal displacements estimated with stable LiDAR points (Fig. 7B) have smaller displacements in the northern block than in the southern block. These displacements have more variations than those calculated with ground points, particularly near the eastern segment of the Baton Rouge fault (Fig. 7A). These differences between results from ground and stable LiDAR points may indicate anomalies close to the fault, but also may be caused by the lack of stable surfaces in some areas in 1999 before rapid urban growth between 2005-2010.

5.2 Comparison LiDAR differencing, time series InSAR and GPS records

InSAR time series and LiDAR differencing indicate that the northern block is subsiding faster than the southern block, with the fault serving as a clear boundary between the uplifting and subsiding zones. The uplift, however, contradicts the long-term displacement of the down-to-south normal fault. Mean subsidence rates from LiDAR differencing (-8.213 - -10.339 mm/y) are one to two orders of magnitude larger than the rates calculated with InSAR time series (-0.552 - -0.732 mm/y) for the northern block (Table 3) clearly indicating the lower accuracy of the LiDAR data. Yet, regional patterns are similar: the northern block is subsiding. Now, our results for the southern block differ between methods. Mean rates from InSAR time series show that this block is mostly uplifting, while LiDAR differencing mean rates indicates that the southern block is subsiding but at a slower rate than the northern block, with some spatial patches of uplift (Table 3, Fig. S1). As explained above, InSAR time series may be affected by seasonal changes, which would bias results to uplift. In the southern block, there are two GNSS stations, 1LSU and SJB1, continuously working since 2004 and 2010, respectively (Fig. 8), but they were mounted on buildings with unknown foundations. GNSS data indicate that this block is experiencing subsidence as indicated by LiDAR differencing, although the rates from GNSS are ~2.5x smaller than the rates from LiDAR, but slightly larger than those from InSAR time series. GNSS indicates that horizontal displacement of the area is to the south-east direction similar to LiDAR differencing. Although the magnitude to the south direction is larger with LiDAR differencing, and smaller to the east direction (-4.471 mm/y to the south and 7.789 mm/y to the east with LiDAR differencing with ground points and -0.63 mm/y to the south and 12.59 mm/y to the east with GNSS data – Table 3).

InSAR time series and LiDAR differencing showed similar results in trends and are comparable to GNSS estimations, which corroborates their usefulness to estimate slow deformation for future studies (Fig. 5-9). LiDAR differencing results have a larger magnitude but have a better spatial resolution, while InSAR time series has better temporal resolution with good spatial resolution compared to point methods such as GNSS. InSAR time series has the advantage of openly available data from different satellites that cover the globe almost completely and there are multiple software options to process the data (e.g., SARscape, ISCE, GMTSAR).

5.3 Relation with anthropogenic activities

Results from LiDAR differencing are estimators for trend motions with good spatial resolution to detect changes in small areas. For instance, construction of the FedEx facility (2014), the Ochsner Medical Complex (2017), the Woman's Hospital (2010), and some new home complexes (2006-2017) are seen in Figures 9C and 9D. We consider that urban growth and new constructions cannot cause this wide and large uplift signal because urban growth has occurred across Baton Rouge including the northern block, where we found multiple examples of new constructions with similar characteristics that do not show this type of uplifting (Fig. S2). The 2000, 2010, and 2020 censuses indicate that the city's population has increased by almost 10% (close to 40.000 new habitants) with most of this increase occurring during the first decade and soon after Katrina when many were displaced (U.S. Census Bureau, 2003; U.S. Census Bureau, 2012; U.S. Census Bureau, 2021). Uplift recorded in LiDAR-differencing is also shown in both InSAR time series, though the last one shows wider uplifting areas.

Using the SONRIS database (n.d.), we counted and categorized wells to know if there is a spatial relationship between wells' locations, construction, and our results. For this analysis, we used wells that were active in any period between 1999 and 2021. Wells that did not have information about starting or ending operation dates were not used. We did not analyze injection pressure or rate of injection or extraction because most of the wells have incomplete information about these data. However, wells that were operating before in the study area can, in some cases, cause delayed pore pressure changes and deform the surface (Shirzaei et al., 2016).

During the study period 2034 water wells were active: 1359 of the wells were in the northern block, and 675 were in the southern block. In total 616 wells extract groundwater for different purposes (Fig. 10), and the remaining 1418 wells monitor groundwater quality mostly near industrial wells, close to areas of injection or oil extraction, and near the western section of the Baton Rouge fault. Most of the groundwater in East Baton Rouge is used for industrial and public supply. These uses are recognized to cause most of the decline of the groundwater levels in the parish (Tomaszewski et al., 2002). Groundwater studies indicate that aquifers in the northern block recharge from water infiltration in areas north of the Denham Springs fault (e.g., Tomaszewski et al., 2002; Vahdat-Aboueshagh and Tsai, 2021). It is known that the withdrawal of groundwater in the Baton Rouge district surpasses the recharge of the aquifers, causing a decline in groundwater levels (White, 2017). The amount of water wells in the northern block is larger for almost all uses than in the southern block (Fig. 10A). Also, most wells are at deeper depths in the northern block (Fig. 10B). Water well data shows that the mean depth of industry and public supply wells is between 400-500 m (1312.34-1640.42 ft), probably reaching the 1500- to 2000-ft sands. These aquifers have been greatly affected by pumping water (Tomaszewski et al., 2002; Nasreen, 2003; Elshall et al., 2013). On the other hand, the southern block has fewer water wells extracting water, but it has injection wells that may cause some uplift by increasing the pore pressure at depth, and the aquifers here receive saline water from the south (Anderson et al., 2013).

Jones et al. (2016) concluded that groundwater withdrawal caused subsidence in the Michoud area in New Orleans, and other studies support this relationship in other areas (eg., Guzy and Malinowska, 2020; Fiaschi and Wdowinski, 2020). They found that areas around chemical plants or refinery facilities with water wells have large subsidence rates. Figure 9B shows the area with the largest subsidence in the study area. This subsidence zone is detected by LiDAR differencing, whereas in InSAR time series it is masked by dense vegetation during the analyzed period. This area does not have water wells, but 12 water wells were active during the study period within a radius of 2 km, eight of which are of domestic use located at the north and east, three for public supply to the west, and one for irrigation also to the west (Fig. S2). Besides this area, we did not find specific water wells linked to anomalous subsidence. Due to the large amount and depth at which the water wells bottom in the northern block in comparison to the water wells in the southern block and considering previous analyses of groundwater withdrawal in the area, our study suggests that the northern block is part of a regional depression cone caused by water extraction. To corroborate this, it is necessary to expand the study area, which is possible to do using SAR data, but the available LiDAR data does not cover the eastern and western portions.

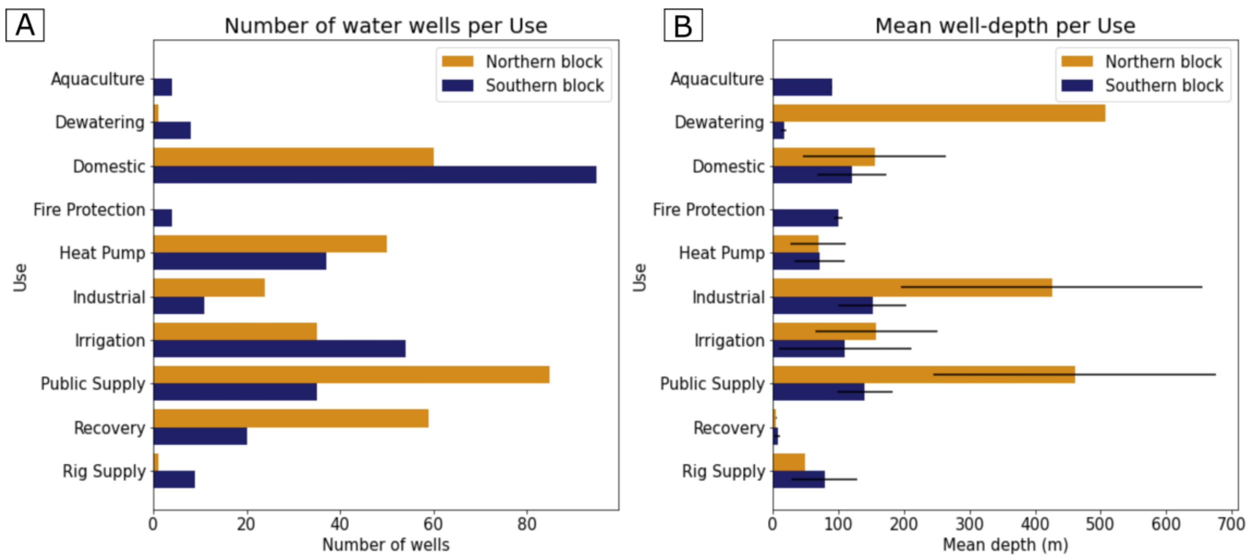

Figure 10: Water wells statistics per block in the study area. **(a)** Number of water wells per use. **(b)** Mean depth of water wells per use, black lines are error bars of one standard deviation. Well data from the Louisiana Department of Natural Resources (SONRIS), (n.d.).

The areas of new construction in Figure 9C and 9D were selected not only because they have the largest uplift signal in the study area but also because most injection wells and oil/gas extraction wells considered for this study are close to or inside these zones (Fig. 1). There are 12 injection wells in the study area, and all are located in the southern block. Nine of these injected salt water at depths between 1470-1975 meters and are in the areas shown in Figures 9C and 9D. The other three inject ozone at shallow depths (~15 m) and are not in any of these areas. Multiple studies have shown that injection can increase pore pressure at depth which can diffuse and cause uplifting (e.g., Shirzaei et al., 2016; Teatini et al., 2011). This increase of pressure can be an explanation for the observed uplift in the southern block.

5.4 Geological factors

The study area has multiple factors that may contribute to vertical crustal movement and are difficult to detangle, but sediment compaction is minimal. Our LiDAR and InSAR results show that the Baton Rouge fault marks the boundary between faster and slower subsiding areas, but we cannot determine whether parts or all of the fault zone slipped episodically or continuously between 1999 and 2020. The rates of differential motion (~3 mm/y) we determine are two orders of magnitude larger than the time-averaged fault slip rate of Shen et al. (2016), These results are comparable to the ~3 mm/y rates along some segments of the Baton Rouge fault reported by Hopkins et al. (2020), suggesting that anthropogenic activities have increased slip rates.

The ICP results from the eastern portion of the Baton Rouge fault shows an apparent change in horizontal displacement direction, but uncertainties are also large. This can be an area for future research because it is also close to two oil fields in the south, these have four injection wells and 11 oil/gas extraction wells that extract from the Siegen field (SONRIS, n.d.). Also, this fault segment is the closest to the study area of Hopkins et al., (2020) (Fig. 2). We cannot conclude much about how the Denham Springs fault is causing subsidence due to the lack of information in the area.

Due to large volumes of groundwater withdrawal in the northern block there is the possibility that some of this saline water is crossing the fault (Nasreen, 2003; Elshall et al., 2013; Anderson et al., 2013) infiltrating some aquifers near the Baton Rouge fault in the northern block. This may explain our general pattern of vertical displacements where subsidence increases from south to north with InSAR time series and LiDAR differencing.

5.5 Future Implications

The vertical crustal motion that occurred during the last two decades detected with InSAR time-series and LiDAR differencing and corroborated by sparse GNSS data can be an indicator of groundwater level and recharge characteristics for the aquifers under the study areas. The aquifers in the northern block are more affected by groundwater extraction. This block has subsidence rates that decrease towards the Baton Rouge fault where saline water infiltrates (Nasreen, 2003; Elshall et al., 2013). The southern block is also undergoing subsidence, but injection causes uplift, and recharge of the aquifers in this block is faster due to saline water flow from southern areas (Fig. 5, 6, 8, 10). Therefore, it is important to perform continuous monitoring at local and regional scales to know how the area is affected by fluid extraction and injection. There are many wells whose purpose is to monitor locally groundwater health, and there are just a few GNSS stations to examine surface changes. This study presents a detailed regional panorama of the relationship between injection and extraction of fluids and vertical surface motion.

East Baton Rouge is one of the most populated parishes in Louisiana and likely its population will grow as has done it for the last 20 years according to the censuses since 2000 (U.S. Census Bureau, 2003; U.S. Census Bureau, 2012; U.S. Census Bureau, 2021). Besides, due to climate changes expected for the ongoing century in the GOM (Pendleton et al., 2010; Frederikse et al., 2020) some population from the Louisiana coastal area probably will migrate to this parish to avoid areas that are at lower elevation and are more vulnerable to flooding (Qiang and Lam, 2016) or after hurricanes, as has happened before (Sastry, 2009). Thus, water consumption probably will increase as the population increases. Considering subsidence as a proxy for groundwater levels, it is important to protect the aquifers underlying the area from saline intrusion and groundwater level decline. These actions will also protect the surface from non-natural vertical changes.

6 Conclusions

We used InSAR time series and LiDAR differencing to evaluate vertical and horizontal crustal movements along the Gulf of Mexico passive margin, including an area of ongoing movement along growth faults between 1999 and 2020. The comparison of methods offers insights into the reliability of differential LiDAR in coastal subsidence. The study area has two listric faults that cut compressed and cemented Pleistocene sediments in the southern Louisiana where sediment compaction is minimal. Extraction and injection wells, groundwater usage, and other anthropogenic activities may influence subsidence and fault slip.

LiDAR differencing can produce trustful results for displacement trends, but LiDAR data must be coregistered to produce accurate results. This method can overestimate displacements, and its accuracy depends on the uncertainty of the available datasets. InSAR time-series are affected by the availability of persistent scatterers in densely vegetated areas and by seasonal changes. Open-source SAR datasets are increasing over time and there will be more sensors in the future (e.g., NISAR) to expand and improve the time series, and enable selective differencing to minimize seasonal factors.

Both methods show that both the footwall and hanging wall of the Baton Rouge fault are subsiding, but the footwall (southern block) is subsiding more slowly. The Baton Rouge fault, therefore, marks a change in vertical crustal movements. LiDAR differencing indicates subsidence with some patches of uplift in the southern block, while the InSAR time series indicates general uplift that reverses the long-term, down-to-the-south displacement, likely InSAR time-series results are affected by hydrological seasonal changes. These trends are consistent with down and southeast motions from the two GNSS stations in the southern block. From the estimated displacement in both blocks we observe creep along the Baton Rouge fault and assume that the fault zone is more permeable and vulnerable to fluid flow than the surrounding areas. Yet, we cannot evaluate the relative contributions of hydrological processes, human intervention, or gravity to the observed fault creep. The Denham Springs fault is not well covered by the LiDAR datasets and shows noise results in the InSAR time series.

Given the proximity of extraction and injection wells to areas of vertical crustal motions, anthropological activities such as groundwater withdrawal and injection of fluids are a more reasonable explanation for our observations than geological factors. Our estimations agree with previous groundwater models in the region that indicate a decline in groundwater levels in the East Baton Rouge parish where we found faster subsidence rates. Decay of groundwater levels can cause subsidence and a depression cone at a regional scale. Areas that are locally uplifting in the southern block are nearby injection wells, suggesting that volumetric expansion due to changes in pressure underground is occurring. Considering the future climate change scenarios where population displacement and water scarcity are likely it is important to consider these observations for future city planning to ensure the conservation and protection of the aquifers in the area, and to minimize the effects of saline incursions.

Acknowledgments

CH and CE were supported by funds from the Marshall-Heape endowment to Tulane University, and from training opportunities offered by UNAVCO.

CH and CE gratefully acknowledge support from the Marshall-Heape endowment to Tulane University. CH thanks the conversations with J. Whitten about the development of this work. This manuscript benefited from conversations with R. Arrowsmith.

Open Research

Data Availability Statement

LiDAR data from 1999 is stored and distributed by the Atlas: The Louisiana Statewide GIS (https://maps.ga.lsu.edu/lidar2000/), and LiDAR data from 2018 is stored and distributed by the USGS Server through the National Map (https://rockyweb.usgs.gov/vdelivery/Datasets/Staged/Elevation/LPC/Projects/USGS_LPC_LA_Amite_2018_LAS_2019/). SAR images from them EnviSAT satellite were retrieved from the Earth Observation Catalogue (https://eocat.esa.int/sec/#data-services-area) and SAR images from Sentinel-1 from the Copernicus Open Access Hub (https://scihub.copernicus.eu/dhus/#/home) both property of the European Space Agency. GNSS information was processed by the Nevada Geodetic Laboratory (http://geodesy.unr.edu/NGLStationPages/gpsnetmap/GPSNetMap.html). The data from water, injection, and extraction wells is stored in the Strategic Online Natural Resources Information System property of the Louisiana Department of Natural Resources (http://sonris-www.dnr.state.la.us/gis/agsweb/IE/JSViewer/index.html?TemplateID=181).

Software availability Statement.

LiDAR data was filtered to create stable surface clouds and DEMs were created using the Point Data Abstraction Library (PDAL, 2018). The ICP algorithm was run using the MATLAB code created by Scott et al. (2020) that uses the LIBICP software (Geiger et al, 2012). The Geomorphic Change Detection software (GCD) was used to create the DoDs (Wheaton et al., 2010). InSAR time series were processed using SARscape (2021) software. Spatial analysis and maps were done with QGIS v. 3.18 (2018).

References

Anderson, C., Hanor, J., Tsai, F., (2013). Sources of Salinization of the Baton Rouge Aquifer System, Southeastern Louisiana. *Gulf Coast Association of Geological Societies Transactions*. 63, 3-12.

Blewitt, G., Hammond, W., Kreemer, C., (2018), “Harnessing the GPS data explosion for interdisciplinary science”. *Eos*, 99, https://doi.org/10.1029/2018EO104623

Blum, M., & Roberts, H. (2012). The Mississippi delta region: Past, present, and future. *Annual Review of Earth and Planetary Sciences*, 40, 655-683. doi:10.1146/annurev-earth-042711-105248

Brook, A., and Ben-Dor, E., (2011). Automatic Registration of Airborne and Spaceborne Images by Topology Map Matching with SURF processor algorithm. *Remote Sensing*, 3 (1), 65-82. doi:10.3390/rs3010065

Chan, Y., Koo, V., (2008). An Introduction to Synthetic Aperture Radar (SAR). *Progress in Electromagnetics Research*, 2, 27-60. doi:10.2528/PIERB07110101

Chan, A., and Zoback, A., (2007). The Role of Hydrocarbon production on Land Subsidence and fault reactivation in the Louisiana Coastal Zone. *Journal of Coastal Research*, 23 (3), 771-786. doi: 10.2112/05-0553

Church, J., Clark, P., Cazenave, A., Gregory, J., Jevrejeva, S., Levermann, A., Merrifield, M., Milne, G., Nerem, R., Nunn, P., Payne, A., Pfeffer, W., Stammer D., and Unnikrishnan, A., (2013). Sea Level Change. In: Climate Change 2013: The Physical Science Basis. Contribution of Working Group I to the Fifth Assessment Report of the Intergovernmental Panel on Climate Change [Stocker, T., Qin, D., Plattner, G., Tignor, M., Allen, S., Boschung, J., Nauels, A., Xia,Y., Bex V., Midgley, P., (eds.)]. Cambridge University Press, Cambridge, United Kingdom and New York, NY, USA.

Crosetto, M., Moserrat, O., Cuevas-Gonzalez, M., Devanthery, N., Crippa, B., (2016). Persistent Scatterer Interferometry: A review. *ISPRS Journal of Photogrammetry and Remote Sensing*. 115, 78-89. doi:10.1016/j.isprsjprs.2015.10.011

Culpepper, D., McDade, E., Dawers, N., Kulp, M., and Zhang, R., (2019a). Synthesis of Fault Traces in SE Louisiana Relative to Infrastructure (Project No. 17GTLSU12). *Transportation Consortium of South-Central States*. https://digitalcommons.lsu.edu/transet_pubs/30/

Culpepper, D., McDade, E., Dawers, N., Kulp, M., and Zhang, R. (2019b). Data from: Synthesis of Fault Traces in SE Louisiana Relative to Infrastructure. Retrieved from https://digitalcommons.lsu.edu/transet_data/30

Dokka, R. Sella, G., and Dixon, T. (2006). Tectonic control of subsidence and southward displacement of southeast Louisiana with respect to stable North America: *Geophysical Research Letters*, 33 (L23308). doi:10.1029/2006GL027250

Dokka, R. (2011). The role of deep processes in late 20th century subsidence of New Orleans and coastal areas of southern Louisiana and Mississippi. *Journal of Geophysical Research*. 116 (B06403). doi:10.1029/2010JB008008.

Durham, C., and Peeples E., (1956). Pleistocene fault zone in southeastern Louisiana. *Gulf Coast Association of Geological Societies Transactions*. 6, 65-66.

Eddy, D., Van Avendonk, H., Christeson, G., Norton, I., Karner, G., Johnson, C., Snedden, J., (2014). Deep crustal structure of the northeastern Gulf of Mexico: Implications for rift evolution and seafloor spreading. *Journal of Geophysical Research: Solid Earth*. 119 (9), 6802-6822. doi: 10.1002/2014JB011311

Elshall, A., Tsai, F., Hanor, J., (2013). Indicator geostatistics for reconstructing Baton Rouge aquifer-fault hydrostratigraphy, Louisiana, USA. *Hydrogeological Journal*. 21 (8), p. 1731-1747. doi: 10.1007/s10040-013-1037-5

European Space Agency, (ESA) (2021a). Earth Observation Catalogue – EO CAT. EnviSAT images. Last visited July/2022. Retrieved from https://eocat.esa.int/sec/#data-services-area

European Space Agency, (ESA) (2021b). Copernicus Open Access Hub. Sentinel-1 images. Last visited July/2022. Retrieved from https://scihub.copernicus.eu/dhus/#/home

Ferretti, A., Prati, C., Rocca, F., (2001) Permanent scatterers in SAR interferometry. *IEEE Transactions on Geoscience and Remote Sensing*. 39 (1), 8–20. doi:10.1109/36.898661

Fiaschi, S., and Wdowinski, S., (2020). Local land subsidence in Miami Beach (FL) and Norfolk (VA) and its contribution to flooding hazard in coastal communities along the U.S. Atlantic coast. *Ocean and Coastal Management*. 187. doi:10.1016/j.ocecoaman.2019.105078

Frederikse, T., Landerer, F., Caron, L. Adhikari, S., Parkes, D., Humphrey, V., Dangendorf, S., Hogarth, P., Zanna, L., Cheng, L., and Wu, Y., (2020). The causes of sea-level rise since 1900. *Nature*. 584 (7821), 393–397. doi:10.1038/s41586-020-2591-3

Gagliano, S., Burton Kemp III, E., Wicker, K., and Wiltenmuth, K., (2003a). Active geological faults and land change in southeastern Louisiana (Contract No. DACW 29-00-C-0034). *U. S. Army Corps of Engineers*. https://biotech.law.lsu.edu/katrina/govdocs/faults.pdf

Gagliano, S., Burton Kemp III, E., Wicker, K., Wiltenmuth, K., and Sabate, R., (2003b). Neo-tectonic framework of southeast Louisiana and applications for Coastal restoration. Transactions of the 53rd *The Gulf Coast Association of Geological Societies and the Gulf Coast Section SEMP*. 262-272

Gasparini, N, Fischer, G, Adams, J, Dawers, N., Janoff, A., (2015) Morphological signatures of normal faulting in low-gradient alluvial rivers in South-eastern Louisiana, USA. *Earth Surface Processes and Landforms*. 41, 642-657. doi: 10.1002/esp.3852

Geiger, A., Lenz, P., and Urtasun, R., (2012). Are we ready for autonomous driving the kitti vision benchmark suite. 2012 IEEE Conference on Computer Vision and Pattern Recognition. 3354-3361. doi: 10.1109/CVPR.2012.6248074. [Computer software] http://www.cvlibs.net/software/libicp/

Goldstein, R., Zebker, H., Werner, C., (1988). Satellite radar interferometry: Two-dimensional phase unwrapping. *Radio Science*. 23 (4), 713-720. doi:10.1029/RS023i004p00713

Guzy, A., Malinowska, A., (2020). State of the art and recent advancements in the modelling of land subsidence induced by groundwater withdrawal. *Water*. 12 (7). doi:10.3390/w12072051

Hoffman, J., Keyes, D., Titus, J., (1983). Projecting Future Sea Level Rise: Methodology, Estimates to the Year 2100, and Research Needs. United States: Strategic Studies Staff, Office of Policy Analysis, Office of Policy and Resource Management, U.S. Environmental Protection Agency. Retrieve from https://repository.library.noaa.gov/view/noaa/10299

Hooper, A., Zebker, H., Segall, P., Kampes, b., (2004). A new method for measuring deformation on volcanoes and other natural terrains using InSAR persistent scatterers. *Geophysical Research Letters*. 31 (23), L23611. doi:10.1029/2004GL021737.

Hopkins, M., Lopez, J., Songy, A., (2021). Coastal Subsidence Due to Faults: Insights from Elevation Profiles of Vehicular Bridges, Southeastern Louisiana, U.S.A. *Journal of Coastal Research*. 38(1), 52-65. doi:10.2112/JCOASTRES-D-21-00015.1

Jankowski, K., Törnqvist, T., Fernandes, A., (2017) Vulnerability of Louisiana's coastal wetlands to present-day rates of relative sea-level rise. *Nature Communication*. 8 (14792). doi:10.1038/ncomms14792

Jones, C., An, K., Blom, R., Kent, J., Ivins, E., and Bekaert, D. (2016). Anthropogenic and geologic influences on subsidence in the vicinity of New Orleans, Louisiana. *Journal of Geophysical Research: Solid Earth*. 121 (5), 3867– 3887. doi:10.1002/2015JB012636

Karegar, M., Dixon, T., Malservisi, R., (2015). A three-dimensional surface velocity field for the Mississippi Delta. Implications for coastal restoration and flood potential. *Geology*. 43 (6), 519-522. doi:10.1130/G36598.1

Karegar, M., Dixon, T., Malservisi, R., Kushe, J., and Engelhart, S., (2017) Nuisance flooding and relative Sea-Level Rise: the importance of present-day land motion. *Science Reports*. 7 (111997). doi:10.1038/s41598-017-11544-y

Karegar, M., Larson, K., Kushe, J., and Dixon, T., (2020) Novel quantifications shallow sediment compaction by GPS Interferometric Reflectometry and implications for flood susceptibility. Geophysical Research Letters. 47 (14). doi:10.1029/2020GL087807

Keogh, M., and Törnqvist, T., (2019). Measuring rates of present-day relative sea-level rise in low elevation coastal zones. *Ocean Science*, 15 (1), 61-73. doi:10.5194/os-15-61-2019

Kuchar, J., Milne, G., Wolstencroft, M., Love, R., Taarasov, L., and Hijma, M., (2018). The Influence of Sediment Isostatic Adjustment on Sea Level Change and Land Motion Along the U.S. Gulf Coast: *Journal of Geophysical Research*, 123 (1), 780-796. doi:10.1002/2017JB014695

Kuecher, G., Roberts, H., and Thompson, M., (2001). Evidence for Active Growth Faulting in the Terrebone Delta Plain, South Louisiana: Implications for Wetland loss and the Vertical Migration of Petroleum. *Environmental Geosciences*, 8 (2), 77-94. doi:10.1046/j.1526-0984.2001.82001.x

Kulp, S., and Strauss, B., (2019). New elevation data triple estimates of global vulnerability to sea-level rise and coastal flooding. *Nature Communications*. 10 (4844). doi:10.1038/s41467-019-12808-z

L3Harris. (2014, November). PS Tutorial – version 0.9. Retrieved April 17, 2022, from https://www.sarmap.ch/tutorials/PS_Tutorial_V_0_9.pdf

L3Harris. (2021, August). PS Tutorial – version 5.6. Retrieved April 17, 2022, from https://www.sarmap.ch/tutorials/PS_v56.pdf

Li, J., Wang, S., Miche, C., Russell, H., (2020). Surface deformation observed by InSAR shows connections with water storage change in Southern Ontario. *Journal of Hydrology: Regional Studies*. 27, 100661- 100672. doi:10.1016/j.ejrh.2019.100661

Lillesand, T. and Kiefer, R., (2000). Remote Sensing and image interpretation. John Wiley & Sons, New York.

Love, R., Milne, G., Tarasov, L., Engelhart, S., Hijma, M., Latychev, K., Horton, B., and Törnqvist, T., (2016). The Contribution of Glacial Isostatic Adjustment to projections of Sea-level change along the Atlantic and Gulf coast of North America. *Earth's Future*. 4 (10), 440-464. doi:10.1002/2016EF000363

Louisiana Department of Natural Resources – Strategic Online Natural Resources Information System (SONRIS), (n.d.). Data of: Oil/Gas wells, Injection wells, and Water wells registration [shp format], last visited June/2020. Retrieved from: http://sonris-www.dnr.state.la.us/gis/agsweb/IE/JSViewer/index.html?TemplateID=181

Louisiana State University - Department of Geography and Anthropology (LSU), (n.d.). LiDAR data distribution by "Atlas: The Louisiana Statewide GIS." [LAS format], Baton Rouge, LA. Last visited: June/2020. Retrieved from: http://atlas.lsu.edu.

Lyons, S., and Sandwell, D., (2003). Fault creep along the southern San Andreas from interferometric synthetic aperture radar, permanent scatterers, and stacking. *Journal of Geophysical Research: Solid Earth*. 108 (B1), 11-24. doi:10.1029/2002JB001831

McCulloh, R., (2001) Active Faults in East Baton Rouge Parish; Louisiana. *Louisiana Geological Survey*. Public information series n. 8. Available at https://www.lsu.edu/lgs/publications/products/public-information-series.php (Accessed: January 2020)

Milliman J., Haq B., (1996). "Sea-Level Rise and Coastal Subsidence: Towards Meaningful Strategies" In: Milliman, J.D., Haq, B.U. (eds) Sea-Level Rise and Coastal Subsidence. Coastal Systems and Continental Margins, vol 2. Springer, Dordrecht. 1-9. doi:10.1007/978-94-015-8719-8_1

Morton, R., Busteri, N., Dennis K. (2002). Subsidence Rates and Associated Wetland Loss in South-Central Louisiana. *Transactions of the Gulf Coast Association of Geological Societies*. 52, 767-778.

Nasreen, M. (2003) The Effect of Faults upon Ground Water Flow in the Baton Rouge Fault System. [master´s thesis]. [New Orleans (LA)] University of New Orleans. Available at https://scholarworks.uno.edu/td/54 (Accessed: 1 June 2022)

National Academies of Sciences, Engineering, and Medicine (NASEM), (2018a). Thriving on OurChanging Planet: A Decadal Strategy for Earth Observation from Space. Washington, DC: The National Academies Press. doi:10.17226/24938.

National Academies of Sciences, Engineering, and Medicine (NASEM), (2018b). Understanding the Long-Term Evolution of the Coupled Natural-Human Coastal System: The Future of the U.S. Gulf Coast. Washington, DC: The National Academies Press. doi:10.17226/25108

National Geodetic Survey (n.d.). Data from: Finding Survey Marks and Datasheets - LA[shp format], last visited January/2020. Retrieved from https://geodesy.noaa.gov/pub/DS_ARCHIVE/BETA_PRODUCTS/

Nerem, R., Beckley, B., Fasullo, J., Hamlington, B., Masters, D., Mitchum, G., (2018). Climate-change–driven accelerated sea-level rise detected in the altimeter era. *Proceedings of the National Academy of Sciences*. 115 (9), 2022-2025. doi:10.1073/pnas.1717312115

Neverman, A., Fuller, I. (2016). Application of Geomorphic Change Detection (GCD) to quantify morphological budgeting error in a New Zealand gravel-bed river: a case study from the Makaroro River, Hawke's Bay. *Journal of Hydrology*. 55 (1), 45-63. Available at https://www.jstor.org/stable/43945085 (Accessed: 21 October 2021)

Nienhuis, J., Törnqvist, T, Jankowski1, K., Fernandes, A, Keogh, M., (2017). A New Subsidence Map for Coastal Louisiana. *GSA Today*. 27 (9), 58-59. doi:10.1130/GSATG337GW.1

Nissen, E., Krishnan, A., Arrowsmith, R., Saripalli, S., (2012). Three-dimensional surface displacements and rotations from differencing pre-and post-earthquake LiDAR point clouds. *Geophysical Research Letters*, 39 (16). doi:10.1029/2012GL052460

PDAL Contributors, (2018). PDAL Point Data Abstraction Library. doi:10.5281/zenodo.2556738

Pendleton, E., Barras, J., Williams, S., Twichell, D., (2010). Coastal vulnerability assessment of the Northern Gulf of Mexico to sea-level rise and coastal change. *U.S. Geological Survey*. Open-File Report. doi:10.3133/ofr20101146

Penland, S. and Ramsey, K., (1990). Relative Sea Level Rise in Louisiana and the Gulf of Mexico: 1908-1988. *Journal of coastal Research*. 6 (2), 323-342. Available at https://www.jstor.org/stable/4297682 (Accessed: 20 Marzo 2021)

Penland, S., Beall, A., and Waters, J., (2001) Environmental atlas of the Lake Pontchartrain Basin. *U.S. Geological Survey*. Open-File Report 02-206. Retrieve from https://pubs.usgs.gov/of/2002/of02-206/intro/toc.html

Pindell, J. Kennan, L., (2009), Tectonic evolution of the Gulf of Mexico, Caribbean and northern South America in the mantle reference frame: An update. In The Origin and Evolution of the Caribbean Plate, *Geological Society, Special Publication*., edited by Lorente, J., Pindell, J. 328, 1–55. doi:10.1144/SP328.1.

Polat, N., Uysal, M., Toprak, A., (2015). An investigation of DEM generation process based on LiDAR data filtering, decimation, and interpolation methods for an urban area. Measurement. *Journal of the International Measurement Confederation*. 75, 50-56. doi:10.1016/j.measurement.2015.08.008

Puskas, C., Meertens, C., & Phillips, D. (2017). Hydrologic loading model displacements from the National and Global Data Assimilation Systems (NLDAS and GLDAS). *UNAVCO Geodetic Data Service Group*.

Qiang, Y., Lam, N., (2016). The impact of Hurricane Katrina on urban growth in Louisiana: an analysis using data mining and simulation approaches. *International journal of Geographical Information Science*. 30 (9), 1832-1852. doi:10.1080/13658816.2016.1144886

QGIS Development Team, 2018. QGIS Geographic Information System. Open-Source Geospatial Foundation Project. [computer software] http://qgis.osgeo.org

SARscape [computer software] (2021). Boulder, Colorado

Sastry, N., (2009). Tracing the Effects of Hurricane Katrina on the Population of New Orleans: The Displaced New Orleans Residents Pilot Study. *Sociological Methods and Research*. 38 (1), 171-196. doi:10.1177/0049124109339370

Sawyer, D., Buffler, R., Pilger Jr., R., (1991), “The crust under the Gulf of Mexico basin” In The Gulf of Mexico Basin, Geological Society of America, ed. by A. Salvador. 53–72. doi:10.1130/DNAG-GNA-J.53

Scott, C., Arrowsmith, J., Nissen, E., Lajoie, L., Maruyama, T., Chiba, T., (2018). The M7 2016 Kumamoto, Japan, Earthquake: 3-D deformation along the fault and within the damage zone constrained from Differential Lidar Topography. *Journal of Geophysical Research: Solid Earth*, 123 (7) 6138-6155. doi:10.1029/2018JB015581

Scott, C., Phan, M., Nandigam, V., Crosby, C., & Arrowsmith, R. (2020). On-Demand 3D topographic differencing implemented in OpenTopography (Version 1.1.0) [Computer software]. https://github.com/OpenTopography/3D_Differencing

Shen, Z., Dawers, N., Törnqvist, T., Gasparini, N., Hijma, M., and Mauz, B. (2017). Mechanism of late Quaternary fault throw-rate variability along the north central Gulf of Mexico coast: implication for coastal subsidence. *Basin Research*. 29 (5), 557-570. doi:10.1111/bre.12184

Shepard, D., (1968). A two-dimensional interpolation function for irregularly spaced data. Proceedings of the 1968 ACM National Conference. 517 – 524. https://doi.org/10.1145/800186.810616

Shirzaei, M., Ellsworth, W., Tiampo, K., Gonzalez, P., Manga, M., (2016). Surface uplift and time-dependent seismic hazard due to fluid injection in eastern Texas. *Science*. 353 (6306), 1416-1419. doi:10.1126/science.aag0262

Simons, M., Rosen, P., (2015). “Interferometric Synthetic Aperture Radar Geodesy.” In Gerald Schubert (editor-in-chief) Treatise on Geophysics, 2nd edition, Vol 3. Oxford: Elsevier. 339-385

Stevenson, D. A., & Agnew, J. D. (1988). Lake Charles, Louisiana, earthquake of 16 October 1983. Bulletin of the Seismological Society of America. 78 (4), 1463-1474. doi:10.1785/BSSA0780041463

Teatini, P., Gambolati, G., Ferronato, M., Serrati, A., Walters, D., (2011). Land uplift due to subsurface fluid injection. *Journal of Geodynamics*. 51 (1), 1-16. doi:10.1016/j.jog.2010.06.001

Tomaszewski, D., Lovelace, J., Ensminger, P., (2002). Water withdrawals and trends in groundwater levels and stream discharge in Louisiana. Louisiana *Department of Transportation and Development, and U.S. Geological Survey*, technical report No. 68.

Turner, R., Rabalais, N., (2018). “The Gulf of Mexico.” In World Seas: An Environmental Evaluation (Second Edition), Academic Press -Elsevier, edited by Sheppard, C, 445-464. doi:10.1016/B978-0-12-805068-2.09994-0

United States Army Corps of Engineers (USACE) (2001). Data from: Raw LIDAR Elevation Data, UTM 15 NAD83, Louisiana FEMA Project - Phase 1: Amite River Basin. last visited June/2020 Retrieve from: https://maps.ga.lsu.edu/lidar2000/

United States Geological Survey (USGS) (2019), USGS Lidar Point Cloud LA Amite 2018, [LAZ format], last visited July/2022. Retrieve from: https://rockyweb.usgs.gov/vdelivery/Datasets/Staged/Elevation/LPC/Projects/USGS_LPC_LA_Amite_2018_LAS_2019/

U.S. Census Bureau. (2003, October). Louisiana 2000 – Population and Housing units counts (Report No. PHC-3-20). Retrieved from https://www2.census.gov/library/publications/2003/dec/phc-3-20.pdf

U.S. Census Bureau. (2012, July). Louisiana 2010 – Population and Housing units counts (Report No. CPH-2-20). Retrieved from https://www2.census.gov/library/publications/decennial/2010/cph-2/cph-2-20.pdf

U.S. Census Bureau. (2021, August). 2020 Population and Housing State Data. Retrieved from https://www.census.gov/library/visualizations/interactive/2020-population-and-housing-state-data.html

Vahdat-Aboueshagh, H., Tsai, F., (2021). Constructing large-scale complex aquifer systems with big well log data: Louisiana model. *Computers and Geosciences*. 148, 104687. doi:10.1016/j.cageo.2021.104687

Walter, J. I., Dotray, P. J., Frohlich, C., & Gale, J. F. (2016). Earthquakes in northwest Louisiana and the Texas–Louisiana border possibly induced by energy resource activities within the Haynesville shale play. *Seismological Research Letters*. 87(2A), 285-294. doi:10.1785/0220150193

Wheaton, J., Brasington, J., Darby, S., Sear, D., (2010). Accounting for uncertainty in DEMs from repeat topographic surveys: improved sediment budgets. *Earth Surface processes and Landforms*. 35 (2), 136-156. doi:10.1002/esp.1886 [computer software] https://github.com/Riverscapes/gcd

Wheaton, J., (2018). Principles of topographic change detection. EarthCube Advancing the Analysis of HRT Workshop Advancing the Analysis of High-Resolution Topography, Broomfield, CO. August 21-24. https://www.youtube.com/watch?v=QIoK52W5sUM&ab_channel=OpenTopography (last accessed November 10, 2020)

White, E. (2017). Water Resources of the Southern Hills Regional Aquifer System, Southeastern Louisiana. *U.S. Geological Survey* Fact Sheet 2017–3010. doi:10.3133/fs20173010

AGU PUBLICATIONS

JGR: Earth Surface

Supporting Information for

Variations in Subsidence along the Gulf of Mexico passive margin from Airborne-LiDAR data and Time Series InSAR in Louisiana

Carolina Hurtado-Pulido[1], Reda Amer[2], Cynthia Ebinger[1], Hayden Holcomb[1]

[1]Department of Earth and Environmental Sciences, Tulane University.

[2]Lamar University, Beaumont, TX

Contents of this file

Figures S1 to S3

Introduction

In Supplementary figure 1 we compare data from the DEMs from 1999 and 2018 and the results from LiDAR differencing from GCD and InSAR time-series with PSI across the profiles shown in Figure 1 on the main text. Supplementary figure 2 shows some examples of constructions on both blocks of the fault showing that constructions are not causing vertical displacement anomalies. Supplemental figure 3 shows the results of both methods in the areas shown in figure 9 compared with the location of injection and extraction wells.

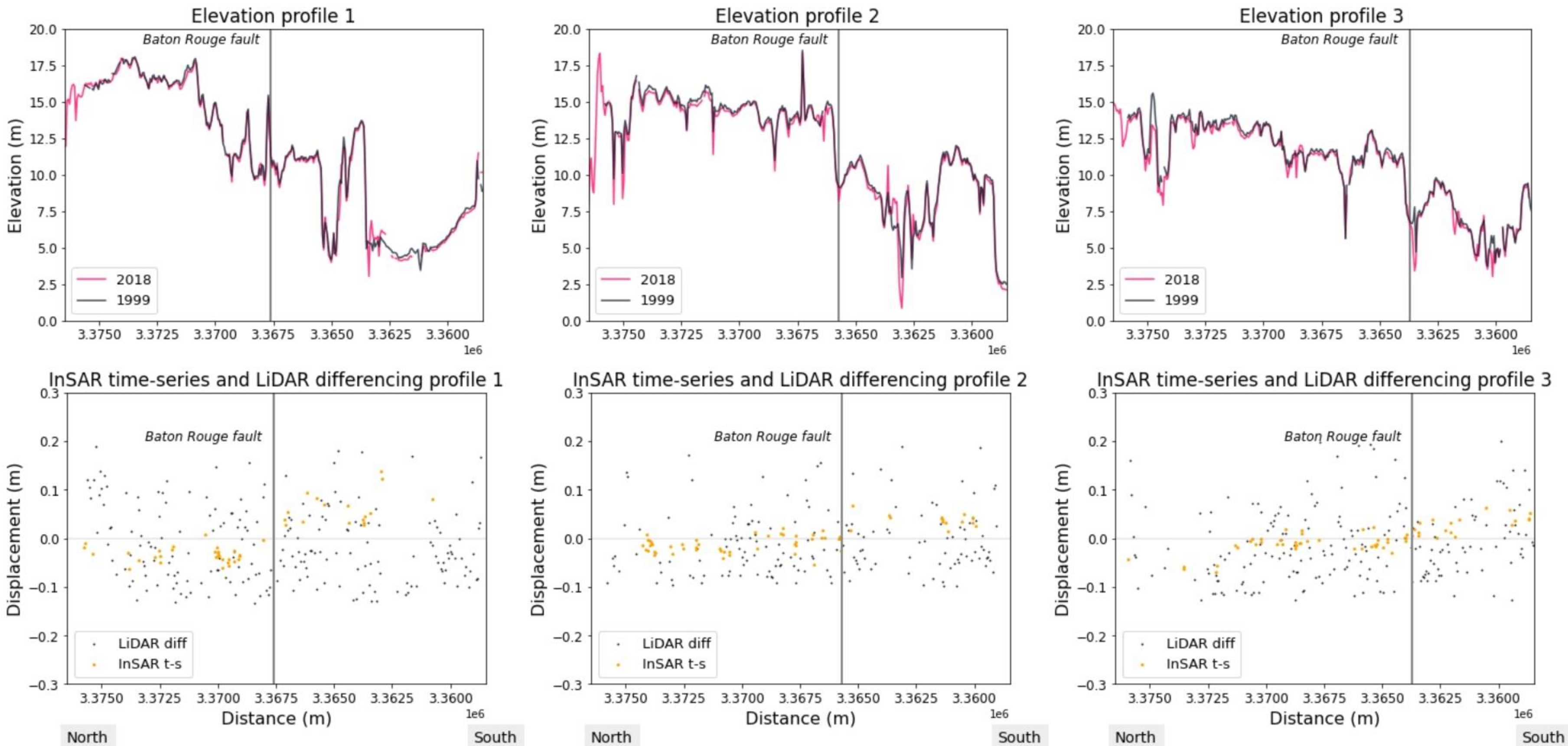

Figure S1. Comparison of elevations using the DEM from 1999 and 2018 in the upper panel and results from our methods along those profiles. For location of the profiles see Figure 1. For the upper profiles, data is averaged every 10 meters from the DEMs, and lower panel is averaged every 20 meters from the GCD results (Fig. 9) and the InSAR time-series for Sentinel-1 results (Fig. 5)

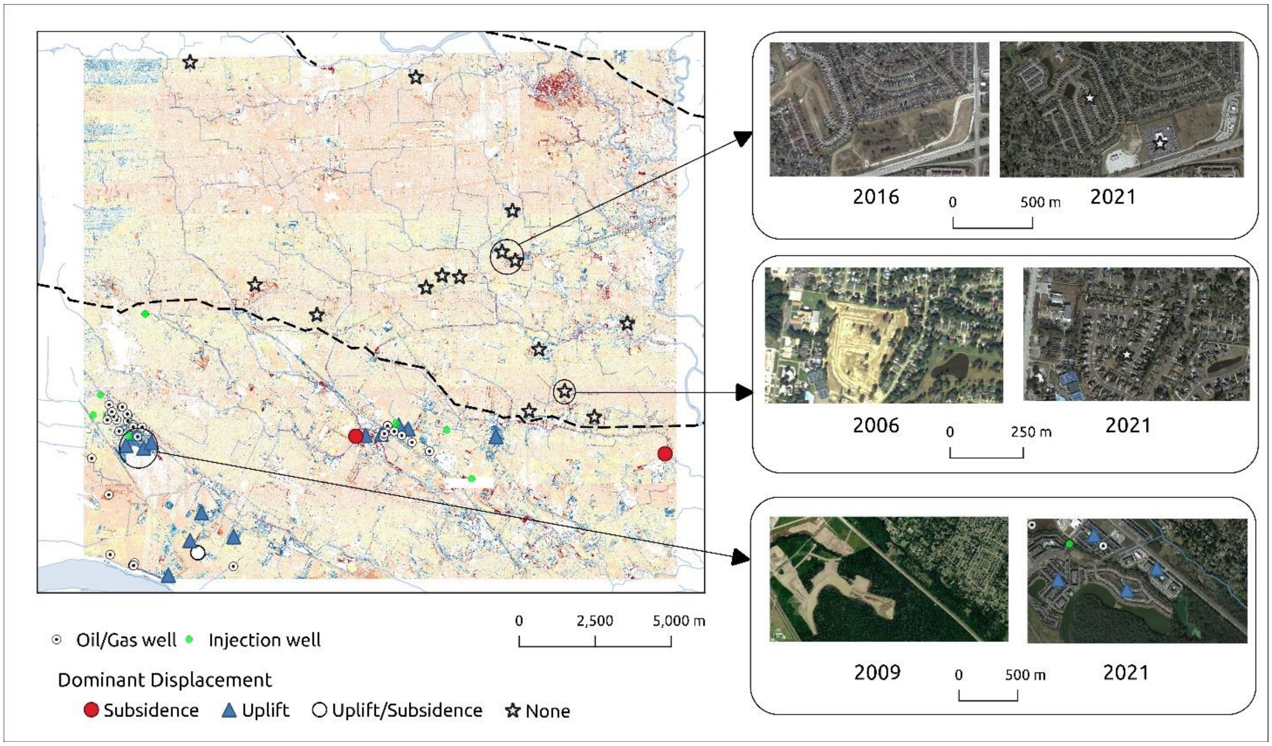

Figure S2. Examples of location of urban constructions built between 1999-2020 and how they look in 2021. Dominant displacement refers to the dominant vertical movement in the area near to the construction. The point labeled as Uplift/Subsidence is the location of Baton Rouge Wastewater Treatment that encounter uplift to the northwest and subsidence to the southeast. Oil/Gas and injection wells are drawn to compare with building constructions near and far from these wells. Legend for displacement is in Figure 9. Images from 2021 taken from QuickMapServices - QGIS (Map data ©2015 Google). Images from past years are taken from the Historical imagery from Google Earth Pro. Well data from the Louisiana Department of Natural Resources (SONRIS), (n.d.).

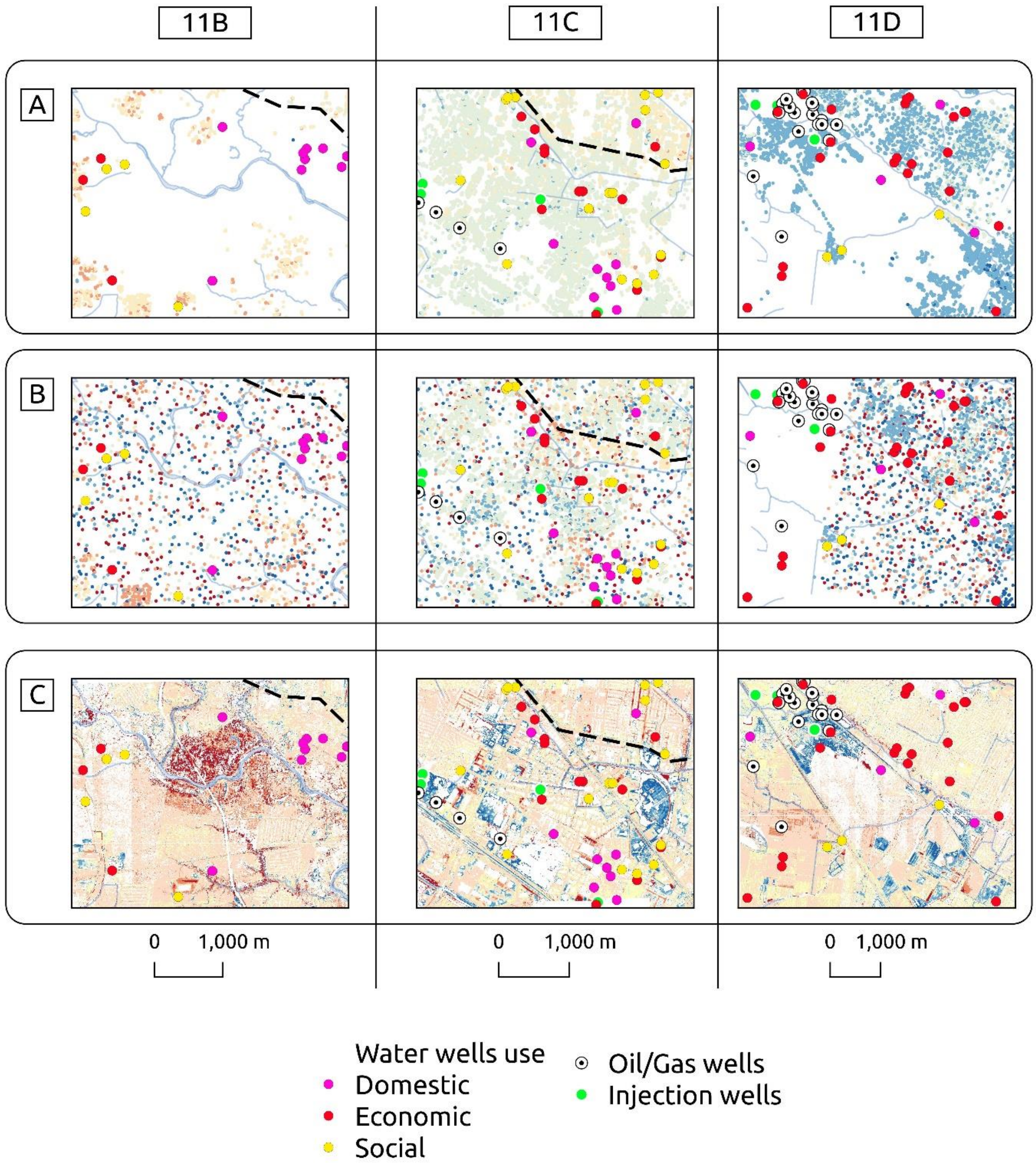

Figure S3. Example of areas experiencing subsidence or uplift determined by different methods compared with injecting and extracting wells. A) Vertical displacement rates calculated with InSAR time series using Sentinel-1 data between 2017-2020. B) Vertical displacement rates calculated with InSAR time series using EnviSAT data between (2004-2010). C) Vertical displacement calculated with LiDAR differencing between 1999-2018. Location of these areas are found in Figure 9. Legend for displacement and rates are in Figures 5 and 9. Well data from the Louisiana Department of Natural Resources (SONRIS), (n.d.

JGR: Earth Surface

Supporting Information for

Variations in Subsidence along the Gulf of Mexico passive margin from Airborne-LiDAR data and Time Series InSAR in Louisiana

Carolina Hurtado-Pulido[1], Reda Amer[2], Cynthia Ebinger[1], Hayden Holcomb[1]

[1]Department of Earth and Environmental Sciences, Tulane University.

[2]Lamar University, Beaumont, TX

Contents of this file

Tables S1 and S2

Introduction

Tables S1 and S2 have extra information about the LiDAR and SAR data not included in the main text.

Table S1:Characteristics for SAR data for ENVISAT and Sentinel-1 (ESA, 2021a, 2021b).

	ENVISAT-ASAR	**Sentinel-1**
Incidence Angle	23° (scene center)	37-39° (center sub-swath 2)
Polarization	Vertical transmit - Vertical receive (VV)	VV
Pixel dimensions (azimuth x range)	5x25 m	14.1x2.3 m
Swath width (km)	5-1150	250
Average coverage along track (km)	100	22.5-22.7
Average coverage across track (km)	56-100	2.7-3.5
Mean Altitude (km)	800	693
Revisit time (days)	35	12
Images used (First and last lines correspond to the start and end of each file in the column list)	ASA_IMS_1PNESA 20040418_161027_000000182026_00083_11159 20040523_161031_000000182027_00083_11660 20050227_161027_000000182035_00083_15668 20050403_161029_000000182036_00083_16169 20060212_161021_000000182045_00083_20678 20060319_161018_000000182046_00083_21179 20070930_161022_000000182062_00083_29195 20071104_161022_000000182063_00083_29696 20071209_161018_000000182064_00083_30197 20080113_161020_000000182065_00083_30698 20080217_161019_000000182066_00083_31199 20080427_161018_000000182068_00083_32201 20080601_161020_000000182069_00083_32702 20080706_161021_000000182070_00083_33203 20081123_161017_000000182074_00083_35207 20081228_161019_000000182075_00083_35708	S1A_IW_SLC__1SDV_ 20170404T000154_20170404T000221_015987_01A5E6_E689 20170428T000155_20170428T000222_016337_01B092_6BCA 20170522T000156_20170522T000223_016687_01BB42_34B3 20170814T000201_20170814T000228_017912_01E0A9_3885 20170919T000202_20170919T000229_018437_01F0B0_A322 20171013T000203_20171013T000230_018787_01FB66_000F 20171106T000203_20171106T000230_019137_020620_3C80 20180105T000201_20180105T000228_020012_022178_B82A 20180210T000200_20180210T000227_020537_02322D_BEC0 20180306T000159_20180306T000226_020887_023D47_EAF0 20180610T000203_20180610T000230_022287_026979_A6AE 20180704T000205_20180704T000232_022637_0273E0_FF2F 20180902T000208_20180902T000235_023512_028F62_FE69 20181113T000209_20181113T000236_024562_02B230_AD1A 20190112T000207_20190112T000234_025437_02D177_FB1A 20190205T000206_20190205T000233_025787_02DE35_6C0A

	20090308_161018_000000182077_00083_36710 20100711_161010_000000182091_00083_43724 _0000.N1	20190313T000206_20190313T000233_026312_02F101_7AC1 20190325T000206_20190325T000233_026487_02F77B_E583 20190430T000208_20190430T000235_027012_030AA6_7891 20190524T000209_20190524T000236_027362_031615_8339 20190629T000210_20190629T000238_027887_032604_1B81 20190723T000212_20190723T000239_028237_033099_4B20 20190828T000214_20190828T000241_028762_0341E0_CA2A 20190921T000215_20190921T000242_029112_034DFB_8DE7 20191027T000216_20191027T000243_029637_03600E_DBC0 20191120T000215_20191120T000242_029987_036C4D_72A0 20191226T000214_20191226T000241_030512_037E76_0DD0 20200131T000213_20200131T000240_031037_0390C2_751B 20200224T000212_20200224T000239_031387_039CE2_AD2E 20200331T000213_20200331T000240_031912_03AF2A_5844 20200424T000213_20200424T000240_032262_03BB79_34AE 20200530T000215_20200530T000243_032787_03CC40_3FB6 20200729T000219_20200729T000246_033662_03E6C3_D4C6 .SAFE

Table S2: Characteristics for LiDAR point clouds from 1999 and 2018.

	1999	**2018**
Instrument	Leica ALS40	Leica ALS70 HP
Altitude (m)	2,438	1,152
Point spacing (m)	4	0.33
Pulse rate (kHz)	15	450
Vertical Accuracy (cm) -RMSE	15	3.6